

DRA/NASA/ONERA COLLABORATION ON ICING RESEARCH
PART II - PREDICTION OF AIRFOIL ICE ACCRETION

William B. Wright
NYMA, Inc.
NASA LeRC Group
Brook Park, Ohio 44142
USA

R. W. Gent
Defence Research Agency
Farnborough Hampshire
ENGLAND

and

Didier Guffond
Office National D'etudes Et de Recherches Aerospatiales
Chatillion
FRANCE

1.0 NOMENCLATURE

c	airfoil chord, m
c_f	skin friction coefficient
c_p	specific heat, J/kg
F	fraction of surface which is wetted.
h_l	laminar convective heat transfer coefficient, $W/m^2\text{°K}$
h_t	turbulent convective heat transfer coefficient, $W/m^2\text{°K}$
k	equivalent sand grain roughness, m
LWC	liquid water content, g/m
MVD	median volume droplet diameter, μm
P_s	static pressure, Pa
P_e	pressure at the edge of the boundary layer, Pa
Pr_t	turbulent Prantl No.
r_h	relative humidity, %
Re_k	local roughness Reynolds No.
s	surface distance from the stagnation point, m
St_k	roughness Stanton No.
T_e	temperature at the edge of the boundary layer, $^{\circ}\text{C}$
T_s	static air temperature, $^{\circ}\text{C}$
V_e	velocity at the edge of the boundary layer, m/s
V_k	velocity at roughness height k , m/s
V_{σ}	shear velocity, m/s
V_{∞}	freestream velocity, m/s
α	angle of attack, degrees
θ_t	momentum thickness, m

ν	viscosity, Ns/m^2
λ	thermal conductivity of air, $\text{W/m}^\circ\text{K}$
μ	viscosity, kg/m/s
σ	surface tension, N/m
τ	shear stress, N/m^2

2.0 SUMMARY

This report presents results from a joint study by DRA, NASA, and ONERA for the purpose of comparing, improving, and validating the aircraft icing computer codes developed by each agency. These codes are of three kinds: 1) water droplet trajectory prediction, 2) ice accretion modeling, and 3) transient electrothermal deicer analysis. In this joint study, the agencies compared their code predictions with each other and with experimental results. These comparison exercises were published in three technical reports, each with joint authorship. DRA published and had first authorship of Part I - Droplet Trajectory Calculations, NASA of Part II - Ice Accretion Prediction, and ONERA of Part III - Electrothermal Deicer Analysis. The results cover work done during the period from August 1986 to late 1991. As a result, all of the information in this report is dated. Where necessary, current information is provided to show the direction of current research.

In this present report on ice accretion, each agency predicted ice shapes on two dimensional airfoils under icing conditions for which experimental ice shapes were available. In general, all three codes did a reasonable job of predicting the measured ice shapes. For any given experimental condition, one of the three codes predicted the general ice features (i.e., shape, impingement limits, mass of ice) somewhat better than did the other two. However, no single code consistently did better than the other two over the full range of conditions examined, which included rime, mixed, and glaze ice conditions. In several of the cases, DRA showed that the user's knowledge of icing can significantly improve the accuracy of the code prediction.

Rime ice predictions were reasonably accurate and consistent among the codes, because droplets freeze on impact and the freezing model is simple. Glaze ice predictions were less accurate and less consistent among the codes, because the freezing model is more complex and is critically dependent upon unsubstantiated heat transfer and surface roughness models. Thus, heat transfer prediction methods used in the codes became the subject for a separate study in this report to compare predicted heat transfer coefficients with a limited experimental database of heat transfer coefficients for cylinders with simulated glaze and rime ice shapes. The codes did a good job of predicting heat transfer coefficients near the stagnation region of the ice shapes. But in the region of the ice horns, all three codes predicted heat transfer coefficients considerably higher than the measured values.

An important conclusion of this study is that further research is needed to understand the finer details of the glaze ice accretion process and to develop improved glaze ice accretion models.

3.0 INTRODUCTION

In 1986 the British Royal Aerospace Establishment (RAE), [now the Defence Research Agency (DRA)], the National Aeronautics and Space Administration (NASA), and the Office National D'etudes Et de Recherches Aerospatiales (ONERA) initiated a collaboration to compare and validate the predictive capabilities of each agency's computer codes that support aircraft icing technology. It was intended that this collaboration would yield a better understanding of the codes and suggest possible improvements to them. The three kinds of

codes compared were 1) water droplet trajectory calculations, 2) ice accretion modelling and 3) transient electrothermal deicer analysis.

Each agency contributed experimental results for the code comparison exercises. The experimental data included droplet collection efficiencies, heat transfer coefficients, and ice accretion shapes. The data were obtained in the following icing facilities: the NASA Lewis Icing Research Tunnel and the NASA Heat Transfer Tunnel in Cleveland, Ohio, USA; the Artington Icing wind tunnel facility near Guilford in Surrey, ENGLAND; and the engine icing facilities at CEPr, Saclay, FRANCE. In addition to comparisons with experimental results, code predictions were mutually compared for hypothetical icing conditions.

Three separate technical reports have been published, one for each of the three kinds of codes. Each report was authored jointly by the three agencies. DRA published and had first authorship of Part I - Droplet Trajectory Calculations (Ref. 1), NASA Part II - Ice Accretion Prediction (the present report), and ONERA Part III - Electrothermal Deicer Analysis (Ref. 2).

These reports documented the joint studies done from 1986 to 1991, and as such, these reports provide the status of each agency's code development during that time period. Since 1991, each agency has been learning more about their codes and continually improving them, and they have also been developing new codes with more capabilities (Ref. 3 - 10).

This present report presents the results of the code comparison exercises for ice accretion on two dimensional airfoils. Section 4 briefly describes the main features of each agency's ice accretion code. All three codes have some common features, such as, a flowfield module, a water droplet trajectory module, a control volume module that performs both a mass balance and a heat balance on the water and predicts ice growth.

The flowfield solutions are obtained from well established flow codes, and the droplet trajectory calculations are described in Reference 1. But this is the only report that describes the heat and mass transfer calculations. Heat transfer over ice surfaces is not well understood (Ref. 11), and therefore Section 4 presents the equations used to calculate the convective heat and mass transfer coefficients and the way that surface roughness is modeled. These methods vary slightly from code to code.

Section 5 describes the experimental databases for both the heat transfer coefficients and the ice accretion shapes. Section 6 presents the heat transfer coefficient comparisons, and Section 6 also presents the ice shape comparisons.

4.0 DESCRIPTION OF THE CODES

Although each code contains the same kinds of modules, these modules may vary from code to code. For example, there are two different flow field modules, three different droplet trajectory integration schemes, three different heat and mass transfer expressions, and three different ways of predicting the ice growth during each time step.

NASA

The LEWICE code (Ref. 3) consists of three main modules as shown in Figure 1: 1) a Hess-Smith 2D potential flow panel method (Ref. 12) to calculate the flow field about an arbitrary two dimensional body, 2) a 2D water droplet trajectory module (Ref. 13) that calculates the water droplet collection efficiency (flux pattern)

on the body, 3) a thermodynamic module that solves the mass and energy balance equations in control volumes, determines the fraction of water that freezes in each control volume, and obtains an ice profile. The energy balance equation, which is based on the derivation by Messinger (Ref. 14), accounts for heat and mass transfer by convection to the freestream, latent heat released during freezing, aerodynamic heating, and incoming and outgoing enthalpy of the water. Ice is assumed to grow normal to the clean airfoil or to the ice surface covering the airfoil.

In LEWICE, the geometry of the 2D airfoil consists of line segments joining a discrete number of coordinates that define the surface. The length of line segments can vary around the airfoil, and smaller segments can be concentrated near regions where the radius of curvature is smallest. The airfoil surface is divided into control volumes that coincide with the line segments.

The calculation starts at the stagnation point, where water droplets enter the control volume (c.v.) via impact at a rate calculated by the droplet trajectory module. A heat balance is made on the c.v., which establishes the freezing rate of water in that c.v. Any water that does not freeze in the first c.v. is assumed to flow downstream to the next c.v., where water also enters by droplet impact. A heat balance is made on the second c.v., and any unfrozen water runs back to the third c.v. The calculation is repeated for successive control volumes until all the water that impacted the airfoil surface either freezes or reaches the trailing edge.

Heat transfer coefficients are calculated from an integral boundary layer analysis described in Ref. 15. The laminar heat transfer coefficient does not depend upon surface roughness, but the transition point and the turbulent heat transfer coefficient are highly dependent on this variable. Transition occurs when the Reynolds number based on the roughness height, Re_k , exceeds 600. The method used to calculate turbulent heat transfer coefficient is described in Ref. 3.

The LEWICE code has a time-stepping capability to grow the ice. With time-stepping, ice accretes on the airfoil for a given time increment, and this ice growth modifies the airfoil leading edge shape. The flowfield is recalculated for the modified airfoil shape, and then the droplet trajectory code is rerun for the new flowfield and the modified airfoil shape. With the new airfoil shape and new collection efficiency as input to the code, another layer of ice is grown, which further modifies the leading edge. This process is repeated for enough time increments to reach the full icing exposure time.

Note: Current (Ref. 10) developments have led to codes for which smaller time steps do provide improved ice shape definition at the cost of additional computer time. LEWICE currently uses an automated time stepping procedure based on limiting the ice growth at each time step

Inputs required by LEWICE include the airfoil geometry, cloud properties such as liquid water content (LWC) and droplet size (or droplet distribution), atmospheric and flight conditions such as freestream velocity (V_∞), static temperature (T_s), static pressure (P_s), humidity (r_h), and angle of attack (α), as well as the total icing time.

ONERA

The potential equation for the flowfield is solved in a "C" grid by using a finite element method (Ref. 16). The code takes the compressibility effect into account but doesn't take the viscous effect into account. Moreover, it cannot determine and compute a boundary layer separation.

The trajectories are computed considering that the only forces to take into account are the drag forces, produced by the velocity differences between the droplet and the flowfield around it.

The determination of the heat transfer coefficient uses the Makkonen (Ref. 17) correlation. The roughness of the profile has only an effect if the boundary layer is turbulent, i.e., the Reynolds number relative to the mean roughness height is greater than 600. The normalized (divided by the chord, c) equivalent sand grain roughness height is a mean value always equal to 0.001.

The code uses the Messinger equations (Ref. 14) to determine the local freezing fraction. Starting at the stagnation point, this code solves the steady state heat balance equation for each successive control volume. It calculates the local equilibrium surface temperature, the freezing fraction and the local rate of freezing. The unfrozen fraction is then allowed to run back to the next control volume.

The ONERA model can be time dependent but generally uses a different method - which is similar to a predictor corrector method - which gives relatively good results: The ice shape is first estimated for a given icing time in one step. The flowfield, the trajectories and the heat transfer coefficient are then calculated on this "estimated shape". Assuming that the values of the local collection efficiency and the heat transfer coefficients are varying linearly from their values on the clean airfoil to their values on the profile covered by the estimated shape, the thermodynamic balance is made and the ice shape calculated. The codes are used twice for all the icing durations.

Inputs required by ONERA include the airfoil geometry, cloud properties such as liquid water content (LWC) and droplet size (or droplet distribution), atmospheric and flight conditions such as freestream velocity (V_∞), static temperature (T_s), static pressure (P_s), and angle of attack (α), as well as the total icing time.

DRA

The DRA ice accretion code, called TRAJICE2, is structured very similar to LEWICE. TRAJICE2 (Ref. 4) uses a two dimensional flow code developed by Fiddes (Ref. 18) coupled with a 2D particle trajectory code to determine the mass of water impacting on the surface. A thermodynamic module evaluates the governing heat and mass balance equations of an iced surface to determine the rate of ice accretion from which an ice profile can be obtained. The heat balance adopted in the DRA code is based on the standard Messinger approach but with both the convective cooling and the evaporative cooling terms modified to allow for compressibility effects. In particular, the changes make the evaporative cooling term more sensitive to the local surface pressure than in the standard Messinger expression. The airfoil is divided into equal-spaced elements for which the ice growth is assumed to be normal to the surface for glaze ice or parallel to the freestream for rime ice. TRAJICE2 is also a time stepping code capable of predicting the ice shape using a single or multiple step process. Heat transfer coefficients are calculated using an integral boundary layer routine similar to LEWICE if it is a multiple time step run or by using correlations for cylinders when using a single time step where the cylinder diameter is an input variable and not necessarily equal to the airfoil leading edge diameter. TRAJICE2 also uses a 50% higher heat transfer coefficient when comparing to tunnel test to account for the higher turbulence in wind tunnels.

Although using multiple time steps should, in principle, be more accurate than a single time step, it was found by DRA that single time steps sometimes gave better comparisons with experiment than did multiple time steps. Furthermore, no determination could be made if there was an optimum time step increment (such as 2 min, 1 min, 30 sec, 20 sec, etc).

Inputs required by TRAJICE2 include the airfoil geometry, cloud properties such as liquid water content (LWC) and droplet size (or droplet distribution), atmospheric and flight conditions such as freestream velocity

(V_∞), static temperature (T_s), static pressure (P_s), and angle of attack (α), as well as the total icing time (Ref. 4,5).

Heat Transfer Analysis

Before the heat transfer comparisons are presented, a brief overview of the heat transfer analysis is presented below. As mentioned previously, NASA and ONERA use the integral boundary layer method exclusively to calculate h , while DRA uses correlations for a cylinder for single time step runs and the integral boundary layer method for multiple time step runs. However, there are a few differences among them which will be noted. It is not the intent of this paper to show the entire derivation of the heat transfer analysis, but merely to highlight the significant terms that affect the calculation of h and to show how the turbulent heat transfer coefficient is highly dependent on the local roughness. A complete derivation of the heat transfer analysis is contained in Appendix B of Ref. 3.

Each code uses a control volume approach to develop its mass and energy balance equations. An airfoil or other body is defined by a discrete number of points which are connected by line segments, each segment defining a control volume. Figure 2 illustrates the mass balance for a clean or iced surface which accounts for water entering and leaving a control volume through impingement of the particles, evaporation, and water from one control volume to the next. The energy balance terms, shown in Figure 3, account for conduction and convection to the freestream, evaporation and aerodynamic heating. The surface roughness, k , is expressed as an equivalent sand grain roughness (more will be said on this later). A thorough discussion of the control volume concept used to formulate the mass and energy balance equations is found in Appendix A of Ref. 3.

The first step in the heat transfer analysis is to define the transition location from laminar to turbulent flow. This is computed by using the following empirical relationship for the local roughness Reynolds number

$$Re_k = \frac{V_k k}{\nu} \quad (1)$$

where V_k is the velocity at the roughness height, k is the equivalent sand grain roughness and ν is the viscosity. For laminar flow, Re_k will be less than 600. When Re_k is greater than 600 the flow is assumed to be turbulent.

Once the transition location is determined, the heat transfer coefficient can be determined for each segment of the airfoil. For laminar flow, Re_k less than 600, the local heat transfer coefficient is calculated using the following equation developed by Smith and Spaulding (ref. 19)

$$h_l = \frac{0.296\lambda}{c\sqrt{Re}} \left[\frac{\left(\frac{V_e}{V_\infty}\right)^{2.87}}{\int_0^{s/c} \left(\frac{V_e}{V_\infty}\right)^{1.87} d(s/c)} \right]^{1/2} \quad (2)$$

where λ is the thermal conductivity and V_e is the velocity at the edge of the boundary layer calculated from the potential flow code.

As shown, the laminar heat transfer coefficient is not dependent on the local roughness. However, for turbulent flow, the heat transfer coefficient is directly dependent on the local roughness and is calculated using a technique taken from Ref. 15 for turbulent flow

$$Nu_t = \frac{\frac{1}{2}c_f Re_x Pr}{Pr_t + \left(\sqrt{\frac{c_f}{2}}\right)/St_k} \quad (3)$$

where Re_x is the local Reynolds number, St_k is the roughness Stanton number, Pr is the Prandtl number, Pr_t is the turbulent Prandtl number, and c_f is the skin friction coefficient. As will be shown later, the value of the roughness, k , can significantly influence h .

To calculate the turbulent heat transfer coefficient one must first calculate the skin friction coefficient and the roughness Stanton number which are also dependent on the local roughness.

The skin friction coefficient is determined by the following equation

$$\frac{c_f}{2} = \left(\frac{0.41}{\log\left(\frac{864\theta_t}{k} + 2.586\right)} \right)^2 \quad (4)$$

where θ_t is the turbulent momentum thickness which can be evaluated by Thwaites formula (Ref. 15).

$$\theta_t = \frac{0.36v^{0.2}}{V_e^{3.29}} \left(\int_0^s V_e^{3.86} ds \right)^{0.8} \quad (5)$$

The roughness Stanton number is determined by the following equation (Ref. 19)

$$St_k = 1.92 Re_k^{-0.45} Pr^{-0.8} \quad (6)$$

The equivalent sand grain roughness is the only variable needed to calculate the heat transfer coefficient that cannot be calculated readily from boundary layer theory. Because of the irregular surface roughness elements associated with an ice surface, none of the existing empirical correlations for equivalent sand grain roughness are valid. Therefore, there have been several correlations which have been developed which are specific to roughness elements on an ice surface. These are described below.

A correlation relating the sand grain roughness to several icing parameters was developed by Ruff and can be found in Ref. 3, Appendix F. This roughness correlation is currently used in LEWICE and was developed in the following manner. To begin with, a set of ice shapes were selected from data taken on a NACA 0012 airfoil by DRA in the Artington icing wind tunnel facility. Next, LEWICE was used to predict the ice shapes for each case by arbitrarily varying the roughness until the best predicted ice shape was obtained. A correlation that relates the equivalent sand grain roughness to the freestream velocity V_∞ , liquid water content (LWC) and the static temperature (T_s) was then developed. The final form of the correlation for the equivalent sand grain roughness is:

$$\frac{k}{c} = \left(\frac{k}{c}\right)_{base} \left(\frac{k}{c}\right)_{LWC} \left(\frac{k}{c}\right)_T \left(\frac{k}{c}\right)_V \quad (7)$$

where c is the airfoil chord and $(k/c)_{base}$ is a baseline value accounting for characteristics that are unique to the facility in which the ice shapes were formed.

Note: The current (Ref. 10) version of LEWICE predicts roughness height from the surface physics, and is not based on the correlation above. See Ref. 8 for a full description. The equation used is

$$k = \left(\frac{4\sigma\mu^2}{\rho F \tau} \right)^{1/3} \quad (8)$$

where σ is the surface tension, μ is the viscosity of water, ρ is the water density, τ is the surface shear stress and F is the fraction of the surface which is wetted. Reference 10 shows good comparisons of this model to measured ice roughness heights.

The DRA uses one of two methods to establish a value for the surface roughness parameter. If an equivalent sand grain roughness can't be estimated, the maximum roughness height of the elements can be used. Typical values range from 0.1 to 5 mm and are input by the user. If a negative value of roughness is specified, the code will automatically calculate the equivalent sand grain roughness by using an empirical relationship similar to that used by LEWICE which is also a function of V_∞ , LWC, and T_s . TRAJICE2 also uses a turbulence level correction factor to calculate the heat transfer coefficient. A multiplication factor of 1.0 or 1.5 is recommended depending on whether the comparisons are made to natural or artificial (i.e., tunnel) icing data, respectively (refs. 4,5). This correction factor is attributed to the higher turbulence levels in icing tunnels. In addition, the DRA uses the cylinder correlation (which requires a single time step) for most of the glaze ice shape predictions shown in this report and uses the integral boundary layer approach (which can use multiple time steps) for the rime cases and the warmest glaze icing conditions.

Initially, k is used to calculate the turbulent Reynolds number for each segment to determine the point of transition from laminar to turbulent flow as governed by Equation 1. If the turbulent Reynolds number is less than 600, the heat transfer coefficient is calculated using Equation 2 which is a function of the edge velocity only. If Re_k is greater than or equal to 600, the heat transfer coefficient must then be calculated using Equation 3 which is highly dependent on the roughness.

5.0 EXPERIMENTAL DATABASE

Below is a brief description of both the heat transfer and ice shape database selected for the DRA/NASA/ONERA collaboration on icing research.

Heat transfer data was taken on four simulated ice shapes which were based on shapes measured in the NASA Lewis 6' X 9' Icing Research Tunnel (IRT) as shown in Figure 4 (ref. 11). The simulated ice shapes were produced by numerically smoothing the original ice shape tracings taken on 2" cylinders to create a symmetrical ice shape about the cylinder axis. The simulated ice shapes were then fabricated out of polyurethane foam and fitted with electrically heated copper strips which were embedded in the foam at closely spaced intervals around the surface of the ice shape. Each copper strip contained a thermocouple which was used to ensure the temperature of the surface was isothermal. The amount of power required to maintain a given surface temperature was then used to determine the heat transfer coefficient of the surface.

Over the years, NASA has compiled a database of ice shapes on various airfoils and other configurations (refs. 20, 21, 22) which have been used for code validation purposes. The majority of ice shape data collected by NASA has been on 21" chord NACA 0012 airfoils. Since temperature is a very important parameter that affects the type and shape of an ice accretion, the ice shape data in Figure 5 (ref. 20) was selected to examine the performance of the three codes as a function of temperature. The two sets of ice shape data, shown in Figure 5, were taken on a NACA 0012 airfoil at 4° angle of attack with the indicated icing conditions. This figure is reproduced from an earlier report (Ref. 21). Not all of the ice shapes shown in this figure were included for this comparison. The first set of ice shapes are for a velocity of 58 m/s and an LWC of 1.30 g/m³. The velocity was increased to 94 m/s with an LWC of 1.05 g/m³ for the second set of ice shapes. As shown in Figure 5, the effect of temperature on the ice shape is clearly seen as the total temperature is increased from -26°C to 0°C. At the coldest temperatures, the ice shapes are completely rime and are streamlined similar to the clean airfoil. The ice shapes become a mixture of both rime and glaze ice with the glaze ice horns becoming more prevalent as the temperature is increased. For temperatures between -26°C and -5°C the mass of ice remains relatively constant. For temperatures warmer than -5°C the total mass of ice accreted begins to decrease until, at 0°C, there is no ice accreted. The decrease in the mass of ice accreted is attributed to water blow-off or water shedding at the warmer temperatures. It is this temperature region that ice prediction codes have difficulty since the modeling of water shedding is either neglected or only approximated in the present models. **Note:** The current (Ref. 10) version of LEWICE has this capability.

An SA13112 airfoil was used by ONERA to obtain experimental ice shapes for various Mach numbers and angles of attack (Ref. 23). From these data, several cases were selected and are shown in Figure 6a. For a Mach number of 0.8, code comparisons were made even though no experimental data was reported by ONERA.

Additional ice shape data for a NACA 0012 airfoil has been reported by the DRA (refs. 24, 25). From these data, several experimental ice shapes were selected for comparison purposes and are shown in Figure 6b. Ice shapes from all three icing facilities were included in this study to determine the effects, if any, of comparing the codes to ice shape data taken from differing icing tunnel facilities.

6.0 RESULTS AND DISCUSSION

The results will be separated into two sections. The first section will present a brief overview of the integral boundary layer method used by all three codes to calculate the heat transfer coefficient (all three ice accretion codes use essentially the same equations to calculate h although there are some differences which will be noted). The calculated heat transfer coefficients from the three ice accretion codes will be compared to experimental values obtained for the four simulated ice shapes shown in Figure 7. The second section will compare ice shape predictions from each of the three ice accretion codes to the experimental ice shape data shown in Figures 5 and 6.

The four simulated ice shapes shown in Figure 7 were used to obtain heat transfer data and were reported by Van Fossen, et al. (Ref. 11). Heat flux gauges were located at the positions shown for each shape. For each of the simulated ice shapes, heat transfer data were taken for both a smooth and roughened surface. A highly polished surface was used for the smooth surface while the rough surface was simulated by introducing grains of sand onto the leading edge of the simulated ice shape surface.

Figures 8 and 9 show the comparison of the heat transfer coefficients calculated by each of the three codes for the 5 minute simulated glaze ice shape with both a smooth and rough surface, respectively. As shown, all three codes predict the heat transfer coefficient reasonably well in the stagnation region, but signifi-

cantly overpredict h near the horns of the ice shape. Aft of the horn region, all three codes do not compare well, probably due in part to inaccurate modeling of the flowfield. Aft of the horn region, there is a large separation/reattachment bubble which has been examined through calculations made with a Navier-Stokes code called ARC2D (Ref. 6). Since none of the codes model the flow separation/reattachment, the resulting calculated flow velocity is larger than the actual velocity in this region.

Figures 10, 11 and 12 show the calculated pressures, velocities and temperatures at the edge of the boundary layer versus the non-dimensional surface distance from the stagnation point for the 5 minute glaze ice shape. As shown, all three codes calculate very similar boundary layer properties. It is interesting to note that each code predicts a large increase in the velocity near the horns of the ice shape while the pressure and temperature plots indicate a significant decrease in pressure and temperature near the horns. This is due to the large drop in the calculated pressure coefficient (not shown) in the horn region which can be attributed to the inaccurate modeling of the flow separation that occurs. Therefore, the calculated flow remains attached and must increase significantly to turn past this region. The net result is significantly higher heat transfer being calculated in this region.

Figure 13 shows the LEWICE calculated heat transfer coefficient for the 5 minute glaze ice shape with a rough surface ($k=0.33$ mm). For s/c values between 0.0 and 0.53, Re_k is less than 600 and the heat transfer coefficient is calculated using Equation 2. In this region, the calculated h compares reasonably well with experiment. For s/c values between 0.53 and 2.10, Re_k is greater than 600 and h is calculated using Equation 3. Notice the large spike in the calculated h at $s/c=0.53$. This is the point where the calculated flow transitions from laminar to turbulent and is evident by the large increase in h from around 100 to 1050 W/m²°K. For s/c values between 0.53 and 2.10, the calculated h does not compare well with experiment. The same calculation was repeated with LEWICE using a $k=1.5 \times 10^{-3}$ mm to simulate a smooth surface. In this case, Re_k is less than 600 over the entire ice shape and h is calculated using Equation 2. Therefore, by merely increasing or decreasing the value of k , one can significantly affect the point of transition from laminar to turbulent as well as the magnitude of h .

Figures 14 and 15 show the experimental and calculated heat transfer coefficients for the 15 minute simulated glaze ice shape with a smooth and rough surface, respectively. In both instances, the calculated h 's compare reasonably well in the stagnation region. In the horn region, DRA and ONERA codes moderately overpredict h , while the NASA calculation which underpredicts h for the smooth surface. Figures 16, 17 and 18 are the calculated values of P_e , V_e and T_e for the 15 minute glaze ice shape. As shown, the three codes predict very similar boundary layer properties for P_e and V_e . The NASA results for T_e are much higher than the results reported by DRA and ONERA. In the horn region of the ice shape, there is a large increase in the velocity and a large decrease in the pressure and temperature as was observed previously for the 5 minute glaze ice shape.

The calculated transition point for the 15 minute glaze ice shape with a rough surface ($k=0.33$ mm) is shown in Figure 19. In this case, the calculated transition point is at $s/c=0.927$. Once again, NASA predicts h reasonably well up to the point of transition. Aft of this region, the calculated h does not compare well with experiment. The calculations were repeated using a $k=1.5 \times 10^{-3}$ mm but no transition point was calculated. Once again, the calculated flow remained laminar over the entire ice surface by using a small value of k .

Heat transfer coefficients for the 15 minute simulated rime ice shape are shown in Figs. 20 and 21 for both a smooth and rough surface, respectively. For the smooth surface, each code significantly underpredicts h up

to the point of flow separation which occurs at the top and bottom of the cylinder. For the rough surface, each code predicts h very well along the entire iced surface up to the point of separation. Figures 22, 23 and 24 show the P_e , V_e and T_e calculated by each code for the 15 minute rime ice shape. Once again, each of the three codes predict very similar boundary layer properties. The calculated transition point for the 15 minute rime ice shape is shown in Fig. 25 for a rough surface. In this case, the transition point occurs at $s/c=0.161$ which is much closer to the stagnation point than the other two cases previously examined. However, unlike the other two cases, LEWICE predicts h in both the laminar and turbulent regions well.

As mentioned previously, DRA uses the cylinder values for many of the glaze ice predictions while NASA and ONERA use the integral boundary layer method throughout. DRA shows that the ice shape prediction is better when the cylinder correlation (a user-selected procedure) is used. Figure 26 shows a comparison of the heat transfer coefficient produced on a NACA0012 airfoil using the integral boundary layer technique and the heat transfer coefficient on a cylinder. The cylinder diameter is chosen so that it is the same as the leading edge diameter of a NACA0012. As seen in this figure, the heat transfer coefficient is much higher for the cylinder. This is to be expected, since cylinder values are symmetric whereas the boundary layer technique gives lower values due to the lower velocities on the pressure surface of the airfoil. Although the coarseness of the experimental data makes any final conclusion open to interpretation, the previous examples show that the integral boundary layer method either predicts or over predicts heat transfer coefficients regardless of which code is used. The cylinder results as shown in Figure 26 exceed the IBL results, so they would be in the direction opposite what is needed to predict the correct HTC value. It appears to illustrate that there is some term missing from all of the codes which would account for this additional heat loss.

Ice Shape Prediction

Each of the three ice accretion codes were used to predict the ice shapes for a selected matrix of experimental ice shapes taken on both a NACA 0012 and an SA13112 airfoil. For each of the 16 cases examined, the experimental ice shapes are indicated with a dashed line and the predicted ice shapes are indicated by a solid line. Table 1 shows a summary of all of the conditions for these cases

Figures 27-36 show comparisons between the experimental and predicted ice shapes for the experimental data of Olsen (Ref. 20) previously shown in Figure 5. In each case, the predicted ice shapes show excellent comparison to experiment except for the mixed glaze condition in Fig. 29.

Figures 27 and 28 show the predicted ice shapes for a velocity of 58 m/s and total temperatures of -26° and -18°C , respectively. These shapes are rime ice shapes, although the ONERA code shows the onset of a small horn formation not seen on the experiment shape or the shape predicted by DRA and NASA.

Figure 29 shows the comparison at -12°C which is a mixed glaze condition. A mixed glaze condition is a transitional case from rime to glaze where the center is glaze ice, but the horns are large rime feathers. In this case, the predicted ice shapes compare reasonably well in terms of ice mass but tend to miss some features of the experimental ice shape. DRA predicts a rime shape for this condition, while NASA and ONERA predict a classic double horn glaze shape. This difference in ice type shows the typical difficulty in predicting this class of shapes.

Figure 30 shows the predicted ice shapes for a total temperatures of -5°C . In this case, the predicted ice shapes are similar to each other and compare well with the experimental ice shapes. DRA shows a larger lower horn than the experiment or the other two codes. It should be noted that DRA used a single time step and a cylinder correlation for this case, which produces a much higher value of heat transfer coefficient on the lower surface as was shown in Figure 26.

Figure 31 shows the prediction at -3°C total temperature. Here, the predictions are smoother than the experimental shape. The predicted horns are not as well developed and the upper impingement is slightly over-predicted, but still the overall shape of the prediction is still very good.

Figure 32 shows the prediction at -1°C total temperature. In this case, each code overpredicts the upper impingement limit even though the general shape and the mass of ice agree reasonably well except for the additional runback ice on the upper surface. This case may illustrate the need to include improved water run-back models which include shedding of excess water from the surface.

The second set of ice shape data, shown in Figure 5, is for a velocity of 94 m/s. Predicted ice shapes for a total temperature of -26°C are shown in Figure 33. DRA compares reasonably well with the experimental ice shape except that they do not predict the pointed leading edge seen on the experimental ice shape. ONERA underpredicts the mass of ice for this case while NASA overpredicts the lower impingement limit and underpredicts the stagnation thickness of ice. For both ONERA and NASA, this is poor prediction for a rime ice case.

Ice shape predictions for a total temperature of -12°C are shown in Figure 34. As opposed to Figure 30, where the cylinder correlation over predicted the horn size, in this case DRA obtained excellent results using its cylinder correlation for heat transfer instead of the integral boundary method. NASA does not predict the correct size of the lower ice horns although it captures the feathers aft of the horn well, while ONERA does not predict the horn angles well. Whether one should use the cylinder correlation or the integral boundary layer approach depends upon the experience of the user, and is not a true reflection of a difference in the codes.

The logic DRA recommends for choice of equivalent cylinder or integral boundary layer method for calculating the heat transfer coefficient distribution is in the first instance to use the cylinder method and single time step approach. If, based on the experience of the user, the predicted shape is unrealistic, then further calculations with the IBL method and multi-stepping approach may be required. There is however at this time no simple procedure as to which method should be used.

Figure 35 shows the predicted ice shapes for total temperatures of -8°C . All three codes predict the upper horn accurately. DRA predicts the lower horn as well where both NASA and ONERA underpredict the lower horn size. Again, this is due to the use of the cylinder correlation and hence is a function of the user's knowledge and experience and is not a reflection of the code capabilities. The cylinder correlation produces much higher heat transfer coefficients on the lower surface as shown in Figure 26. However as shown in Figs. 8, 9, and 13-15, the integral boundary layer method overpredicts experimental heat transfer results. This discrepancy illustrates some physical phenomena which is not properly handled by any of the codes.

Figure 36A shows the prediction at -2°C total temperature. The upper horn angle is well predicted by the codes, but there are some small differences in the size of the horn as the ONERA prediction gives slightly larger horns while the DRA predicts slightly smaller horns than the experiment. Once again, DRA shows superior prediction on the lower horn due to the higher heat transfer coefficient produced by the cylinder correlation. Both NASA and ONERA predict a smaller horn with more runback refreezing. Once again, since an iced airfoil does not resemble a clean cylinder, this result shows that there is some physical phenomena which is not properly handled by any of the codes. Figure 36B shows a more direct comparison of the codes, as DRA used its integral boundary layer method instead of the cylinder correlation. In this case, the DRA prediction shows the same characteristics as the NASA and ONERA predictions.

Figures 37-39 show comparisons between the predicted and experimental ice shapes for the DRA data (shown in Figure 6) taken on a 0.152 m chord NACA 0012 at 0°C and 8.5° angle of attack and for a beak ice shape on a 0.465m chord NACA 0012 at 8° angle of attack. As shown in Figure 37, for the 0° angle of attack

case, all of the codes underpredict the leading edge thickness of ice shown in the experiment, with NASA underpredicting the shape by the greatest amount. Due to the large, thin rime feathers on the experimental ice shape, this may be due to the ice density values used by the codes. Rime ice can have ice densities as low as 100 kg/m^3 as opposed to a value of 917 kg/m^3 for glaze ice. DRA again increases the heat transfer coefficient by using its cylinder correlation. NASA and ONERA predict similar thicknesses at the stagnation point which is approximately half of the ice growth shown for the experimental ice shape. ONERA predicts much larger horns than the other codes or the experiment. The predicted horn angle is larger as well. NASA underpredicts the entire mass. Since ONERA is modelling more of the compressible nature of the flow at this high mach number case, it should produce an ice shape closer to the experiment.

Figure 38A shows the comparison for the 8.5° angle of attack case. On the upper surface, all three codes predict a lower horn angle than the experiment and a further extent of ice impingement than the experiment. Due to the high angle of attack, DRA suggests that the flow was stalled on the airfoil for this case. Stall behavior can not be modeled by any of the flow codes, but its effect can be approximated by running the case at a lower angle of attack. DRA ran the same conditions in Figure 38A, but changed the angle of attack until the predicted ice shape matched the ice shape in the experiment. This result is shown in Figure 38B where a 2° angle of attack was used.

The improved agreement shown in Figure 38B between the predicted results and experiment supports the DRA theory that the airfoil may have stalled. At present with the existing codes, there is no way of predetermining if the ice accretion will cause the airfoil to stall. Hence all users of the codes should be aware of the potential danger of significant errors in the predicted ice shapes when making a prediction on an airfoil at a high angle of attack. Additionally, DRA used a single time step and a cylinder correlation for heat transfer coefficient to predict the shape shown in Figure 38A, but used multiple time steps and the integral boundary layer method for the shape in 38B as these produced the best prediction each time. Again, it would be advantageous if a method existed which could ascertain which model to use for design conditions for which there is no experimental data.

Figure 39 shows the comparison for a beak ice condition at 8° angle of attack and a total temperature of 4.7°C . There is no experimental data at this condition. All of the codes predict similar ice shapes, with ONERA predicting the largest beak horn and DRA predicting the furthest aft extent.

Figure 40 shows the predicted ice shapes for a 0.6 m chord SA13112 airfoil at $M=0.25$ and 10° angle of attack. As shown all three codes do a poor job of predicting the ice shape. However, there are several similarities between the three predicted ice shapes. First, each code predicts a large horn near the leading edge of the airfoil. Second, each code predicts a fair amount of ice on the lower surface of the airfoil. The predicted ice shapes are typical ice shapes that would be expected for an angle of attack of 10° yet the experimental ice shape looks more like an ice shape accreted at 2° . This would again indicate a condition for which the flow has stalled. DRA again parameterized angle of attack and again determined that the angle of attack which best fits the experiment is 2° . This shape is shown in Figure 40B. DRA was consistent in again using a single time step for the original angle of attack and multiple time steps for the stalled angle of attack. Note that although the case shown in Figure 38A was an 8° angle of attack condition and the case shown in Figure 40A is a 10° angle of attack condition, the stalled angle of attack was again 2° . Higher accuracy flow codes such as Naviér-Stokes would be needed to better predict these ice shapes without artificially reducing the angle of attack.

Figure 41 shows the predicted ice shapes for a SA13112 airfoil at $M=0.50$ and 0° angle of attack. All three codes predict ice much further back than shown on the experiment. This can again be attributed to the use of low complexity flow solvers which allow particles to impinge aft of ice horns. Both NASA and ONERA predict a clean leading edge while DRA matches the stagnation ice thickness due to their use of higher heat transfer

coefficient values. Both DRA and ONERA predict the horn size, with a horn angle which is slightly larger than the experiment while NASA underpredicts the ice shape throughout.

Figure 42 shows the predicted ice shapes for a SA13112 airfoil at $M=0.8$ and 10° angle of attack for which there is no experimental data. For this case, all three codes show similar double horn glaze ice shapes. Similarly to the other conditions, NASA and ONERA match closely in the stagnation region, while DRA has more ice throughout.

7.0 CONCLUSIONS/RECOMMENDATIONS

Each of the three ice accretion codes were used to predict ice shapes for a selected matrix of experimental ice shapes. All three ice accretion codes did a reasonable job of predicting the ice shapes. For each of the experimental ice shapes examined, one of the three ice accretion codes (LEWICE, ONERA or TRAJICE2) predicted the general features of the experimental ice shape (i.e. shape, impingement limits, mass of ice) better than the other two. Additional comparisons were made to heat transfer data taken on three simulated ice shapes. All three codes were judged to compare reasonably well with the experimental heat transfer data in the stagnation region of the ice shapes. In the horn region of the ice shapes, all three codes tend to overpredict the heat transfer coefficient, sometimes quite significantly. Several reasons for this may be the increased velocities calculated by the potential flow code around the horn region and/or an inaccurate roughness correlation contained in the model.

The results of the codes can also be improved significantly by altering the user input, as indicated by the difference between the one step and multi-step results provided by the DRA. For this reason, this code requires a degree of user experience in order to achieve the optimum accuracy. Also, the codes used in this report are unlikely to provide good agreement with experimental ice shapes formed on an airfoil at a high angle of attack (e.g. $\geq 8^\circ$) because aerodynamic stall caused by the ice accretion is neglected in these models. Selective use of cylinder correlations despite concerns about the accuracy of the resulting heat transfer coefficient, as well as use of reduced angles of attack in stall conditions can greatly improve the predictions of the ice shape. Unfortunately, there is no methodology for determining the use of either correction for cases where the ice shape is not known beforehand.

The following recommendations are made in support of an ongoing collaboration between NASA/ONERA/DRA to validate an upgrade future ice accretion codes:

1. Additional comparisons be made to ice shape data taken on other airfoils and from other icing facilities.
2. Additional experimental heat transfer data is needed to assess the accuracy of the existing codes.
3. Quantitative data on ice roughness is needed to establish better estimation of the equivalent sand grain roughness parameter k .
4. Additional research into the aerodynamic effects of icing which can then be used for future improvement of ice accretion models.

8.0 REFERENCES

1. Gent, R.W., Guffond, D., and Reinmann, J., "DRA/NASA/ONERA Collaboration on Icing Research: Part I - Prediction of Water Droplet Trajectories," DRA/MS/TR93085/1, Dec. 1993.
2. Guffond, D., Reinmann, J. Gent, R.W., "DRA/NASA/ONERA Collaboration on Icing Research: Part III - Prediction of Thermal Deicer Simulations," ONERA T.R. 2/7766 PN, June 1993.

3. Ruff, Gary A. and Berkowitz, Brian M., "User's Manual For The NASA Lewis Ice Accretion Prediction Code (LEWICE)," NASA CR-185129, May 1990.
4. Gent, R.W., "TRAJICE2 - A Combined Water Droplet Trajectory and Ice Accretion Prediction Program for Aerofoils," RAE-TR-90054, November 1990.
5. Gent, R.W., "HOVACC - An Aerofoil Ice Accretion Prediction Program for Steady, Two-Dimensional, Compressible Flow Conditions," RAE-TR-88052, August 1988.
6. Potapczuk, M.G., and Gerhart, P.M., "Progress in Development of a Navier-Stokes Solver for Evaluation of Iced Airfoil Performance," AIAA-85-0410, January 1985.
7. Wright, W. B., "Advancements in the LEWICE Ice Accretion Model," NASA CR191019 (AIAA-93-0171), Jan. 1993.
8. Wright, W.B., "Update to the NASA Lewis Ice Accretion Code LEWICE," NASA CR195387, Oct. 1994.
9. Wright, W. B. and Bidwell, C. S., "Additional Improvements to the NASA Lewis Ice Accretion Code LEWICE," NASA TM (AIAA-95-0752), Jan. 1995.
10. Wright, W.B., "Users Manual for the Improved NASA Lewis Ice Accretion Code LEWICE 1.6," NASA CR198355, June 1995.
11. Van Fossen, G.J., Simoneau, R.J., Olsen, W.A. Jr., and Shaw, R.J., "Heat Transfer Distributions Around Nominal Ice Accretion Shapes Formed on a Cylinder in the NASA Lewis Icing Research Tunnel," NASA TM-83557, January 1984.
12. Hess, J. L. and Smith, A. M. O., "Calculation of Potential Flow About Arbitrary Bodies," Progress in Aeronautical Sciences, 8:1-138, (D. Kuchemann, editor), Elmsford, New York, Pergmon Press, 1967.
13. Frost, W., Chang, H., Shieh, C. and K. Kimble, "Two Dimensional Particle Trajectory Computer Program," Interim Report for Contract NAS3-224488, 1982.
14. Messinger, B.L., "Equilibrium Temperature Of An Unheated Icing Surface as a Function of Airspeed," Journal of Aeronautical Sciences, Vol. 20, Jan. 1953, pp. 29-42.
15. Kays, W. M. and Crawford, M. E., Convective Heat and Mass Transfer. 2nd edition, MacGraw-Hill Book Company, New York, 1980.
16. Bredif, M., "A Fast Finite Element Method for Transonic Potential Flow Calculations," AIAA 83-0507, January 1983.
17. Makkonnen, L., "Heat Transfer and Icing on a Roughened Cylinder," National Research Council of Canada, Report 23312, 1984.
18. Fiddes, S.R., DRA unpublished work.
19. Smith, A.G., and Spalding, D.B., Journal of Royal Aeronautical Society, Vol. 62, pp. 60-64, 1958.

20. Olsen, W.A. Jr., Shaw, R.J. and Newton, J., "Ice Shapes and the Resulting Drag Increase for a NACA 0012 Airfoil," NASA TM-83556, January 1984.

21. Shaw, R.J., Sotos, R.G., and Solano, F.R., "An Experimental Study of Airfoil Icing Characteristics," NASA TM-82790, January 1982.

22. Potapczuk, M.G., and Berkowitz, B.M., "An Experimental Investigation of Multi-Element Airfoil Ice Accretion and Resulting Performance Degradation," NASA TM-101441, January 1989.

23. Guffond, D., "Wind Tunnel Study of Icing and De-Icing Oscillating Rotor Blades," 8th Helicopter European Forum, September 1982.

24. Gent, R.W., and Beauchamp, A.R., "Experimental Ice Shapes for Validation of a Theoretical Ice Accretion Prediction Program," RAE-TR-86025, May 1986.

25. Gent, R.W. and Beauchamp, A.R., "Experimental Ice Shapes for Validation of a Theoretical Ice Accretion Prediction Program - Part II," RAE-TR-88039, May 1988.

Table 1 - Ambient and Flight Conditions Used
for Ice Shape Predictions in Figures 27 - 42

Figure Number	Airfoil	Chord m	Angle of Attack degrees	Velocity m/s	Static (Total) Temperature °K	Static (Total) Temperature °C	Pressure KPA	Humidity %	LWC g/m³	MVD microns	Exposure Time seconds
NASA Cases											
27	NACA0012	0.530	4.0	58.10	245.2	-27.8 (-26.0)	95.61	100.0	1.30	20.0	480.0
28	253.2	-19.8 (-18.0)
29	259.1	-13.9 (-12.0)
30	266.3	-6.7 (-5.0)
31	269.1	-3.9 (-2.0)
32	270.2	-2.8 (-1.0)
33	.	.	.	93.89	242.5	-30.5 (-26.0)	92.06	.	1.05	.	372.0
34	256.4	-16.6 (-12.0)
35	260.8	-12.2 (-8.0)
36	266.4	-6.6 (-2.0)
DRA Cases											
37	.	0.152	0.0	130.50	260.7	-12.3 (-3.8)	90.50	.	0.50	17.5	120.0
38	.	.	8.5	.	260.7
39*	.	0.405	8.0	131.50	269.1	-3.9 (4.7)	85.00	.	0.60	20.0	180.0
ONERA Cases											
40	SA13112	0.600	10.0	81.30	236.0	-10.0 (-6.7)	79.5	.	0.50	20.0	900.0
41	.	.	0.0	162.50	.	.	2000m altitude	.	.	.	450.0
42*	.	.	0.0	249.90	243.0	-30.0 (-1.2)	180.0

* No Experimental Data Available

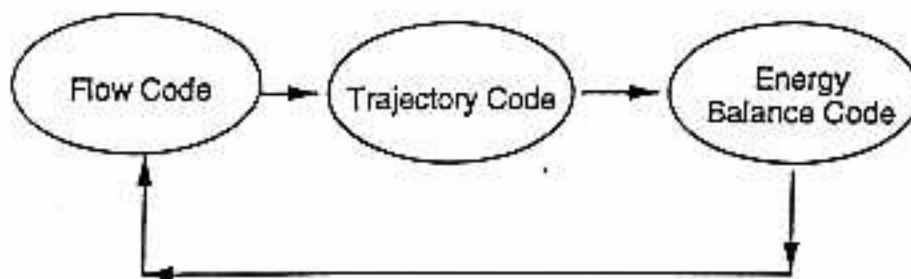


Figure 1 – Modules of an Icing Code

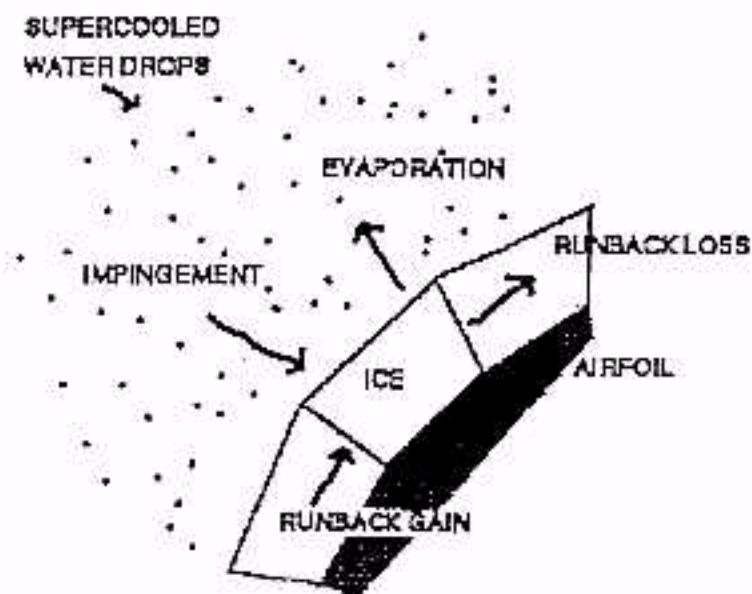


Figure 2 – Mass Balance on a Control Volume

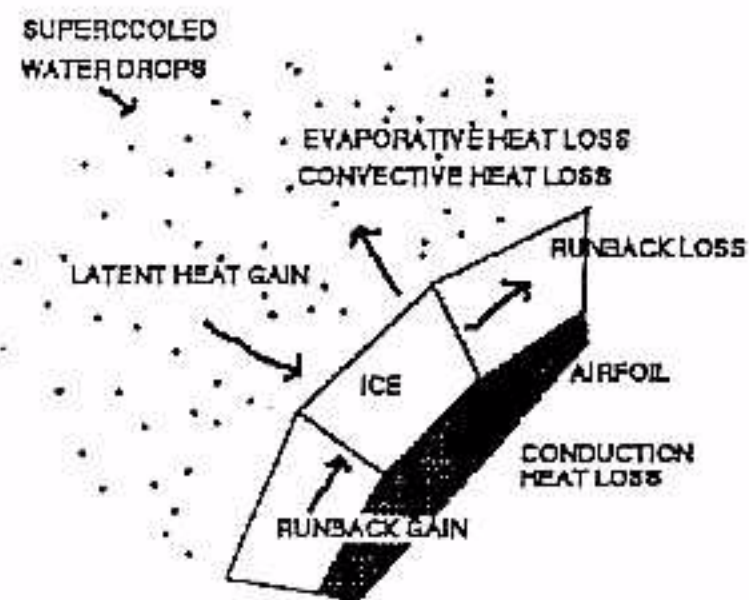


Figure 3 – Energy Balance on a Control Volume

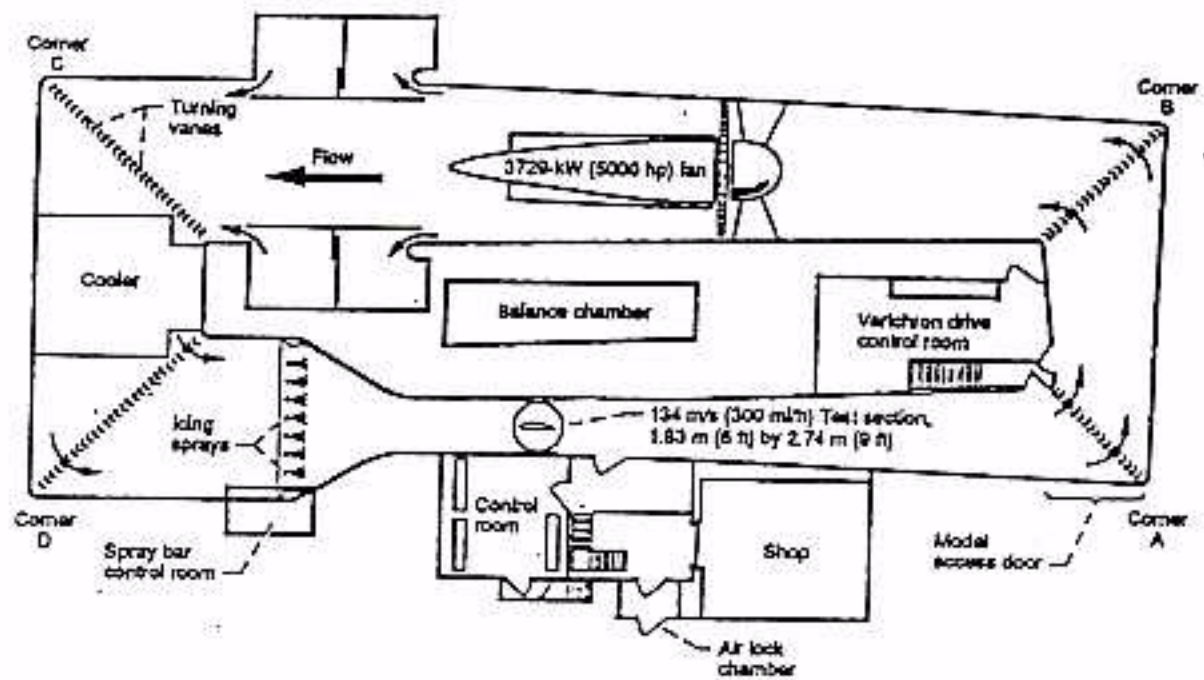


Figure 4 – NASA Lewis Icing Research Tunnel

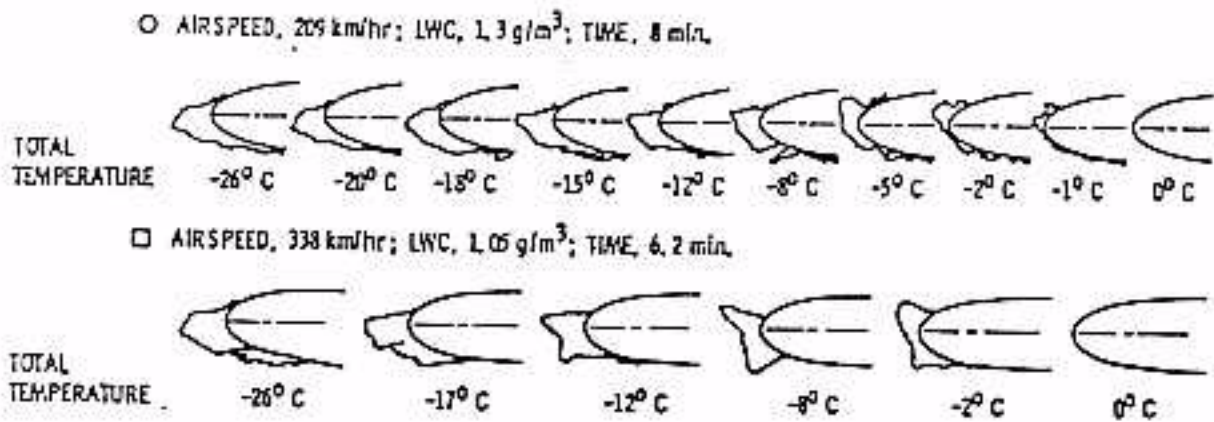


Figure 5 – Summary of NASA Ice Shapes

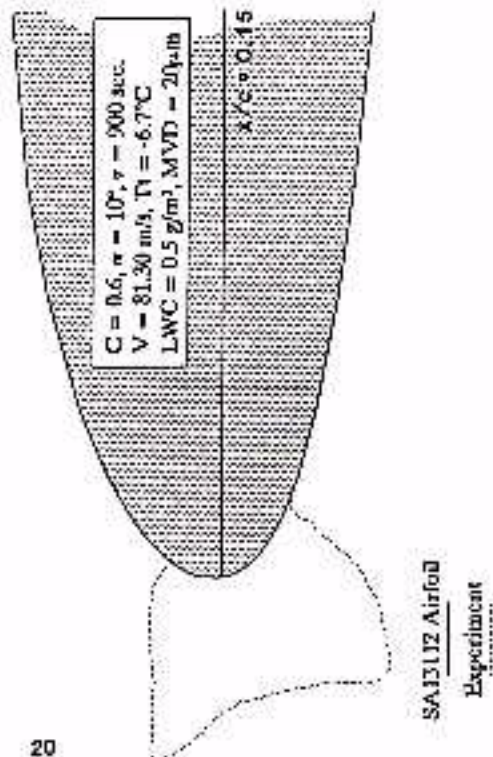
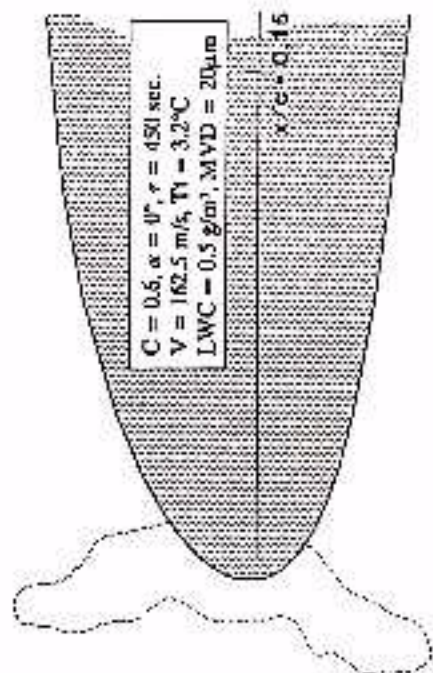


Figure 6(a) ONERA Icing Data

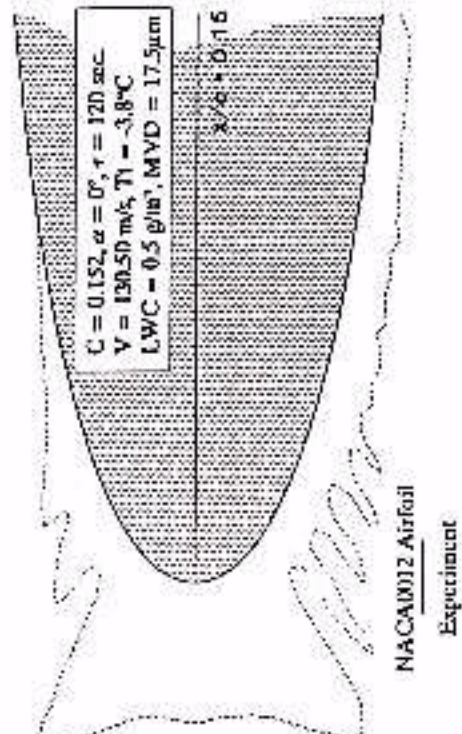
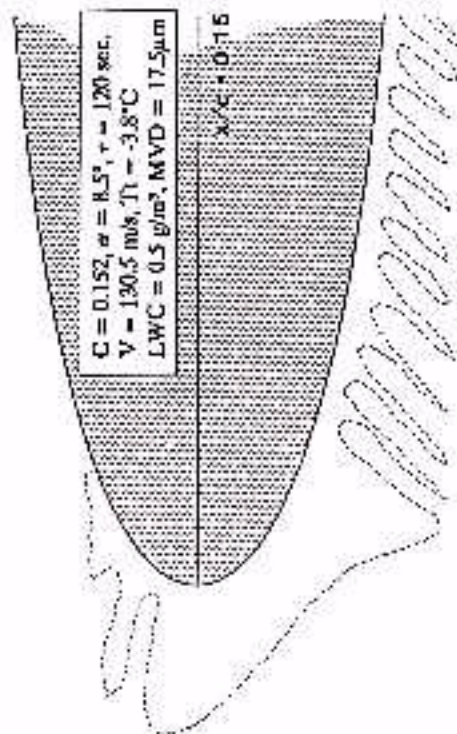
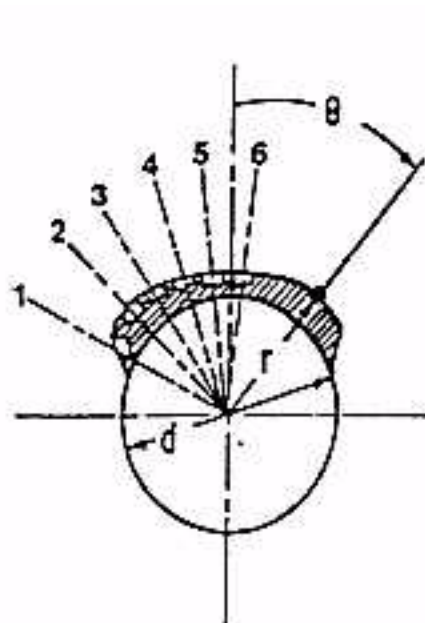
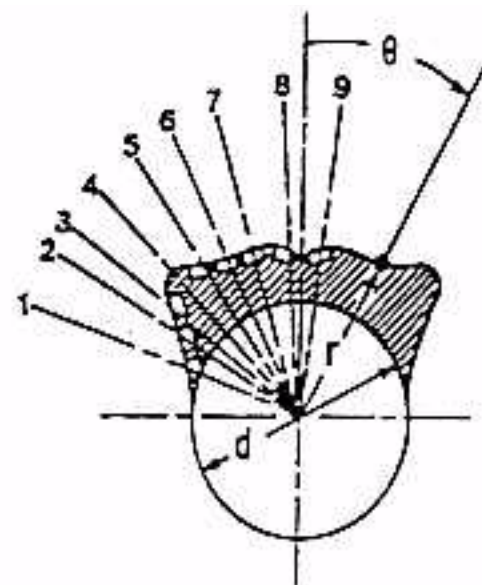


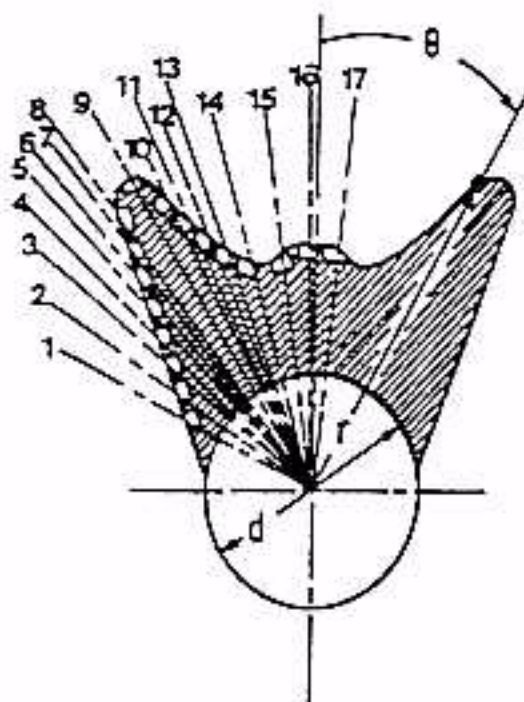
Figure 6(b) DRA Icing Data



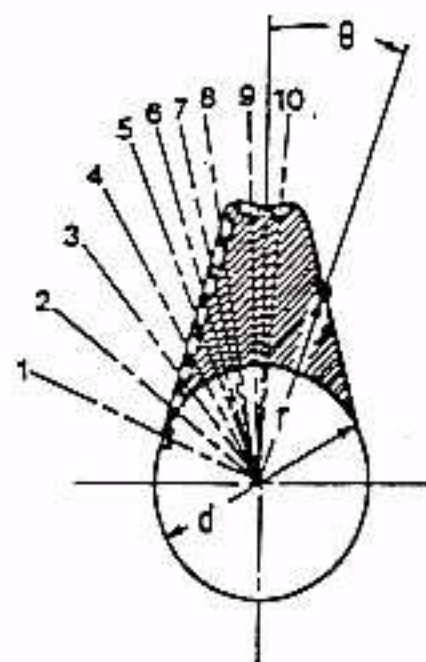
(a) Two minute glaze ice



(b) Five minute glaze ice



(c) Fifteen minute glaze ice



(d) Fifteen minute rime ice

Figure 7 – Ice shape cross sections showing profile coordinates and heat flux gage locations

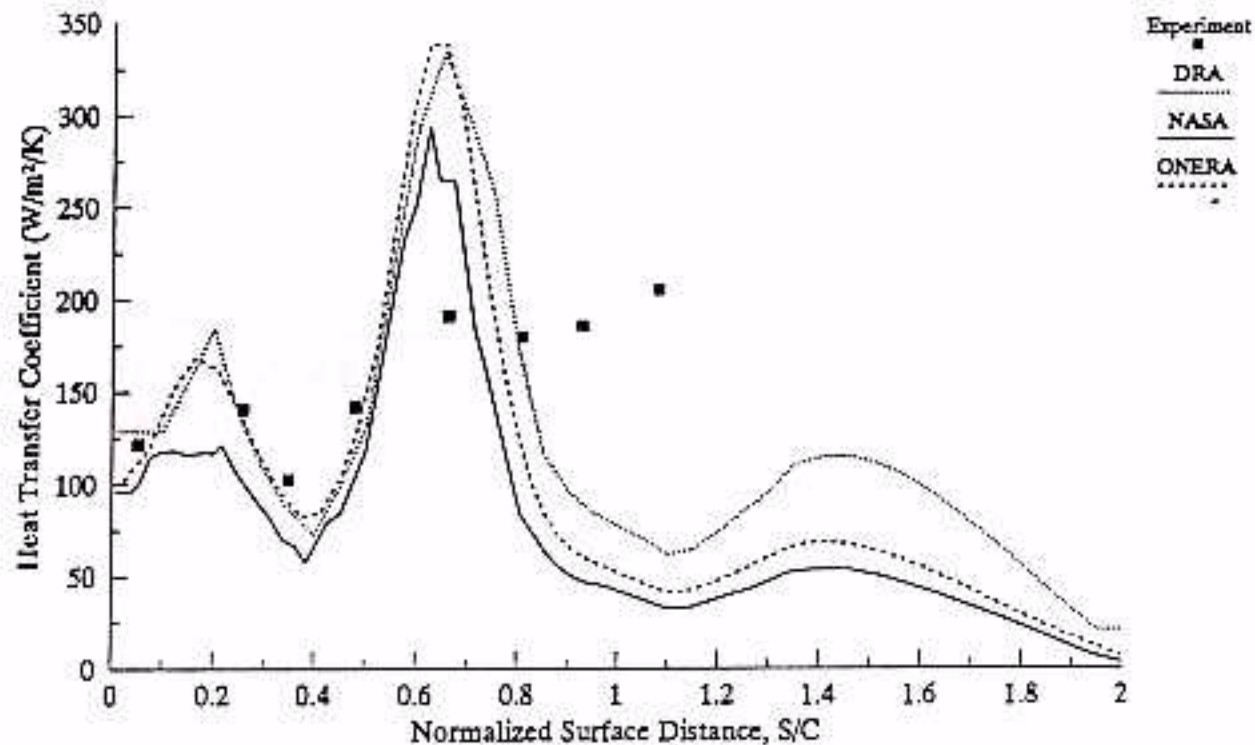


Figure 8 - 5 min Glaze Iced Cylinder
(Smooth Case)

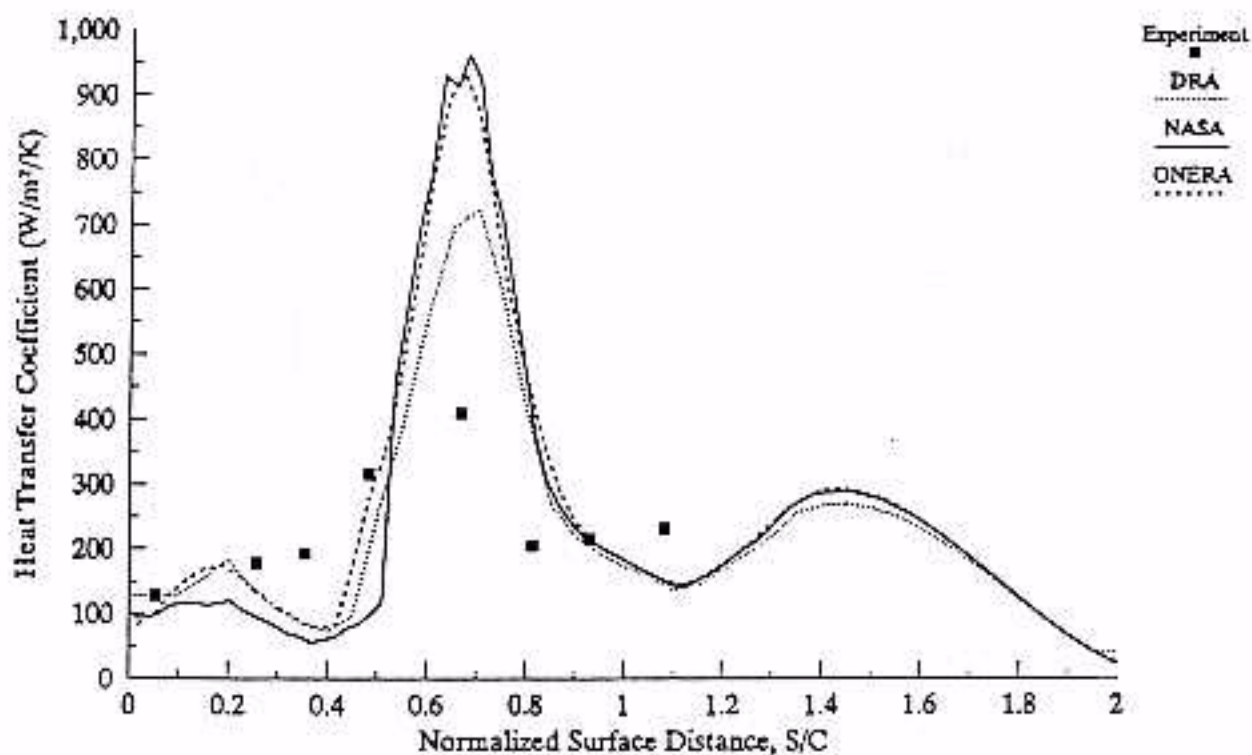


Figure 9 - 5 min Glaze Iced Cylinder
(Rough Case)

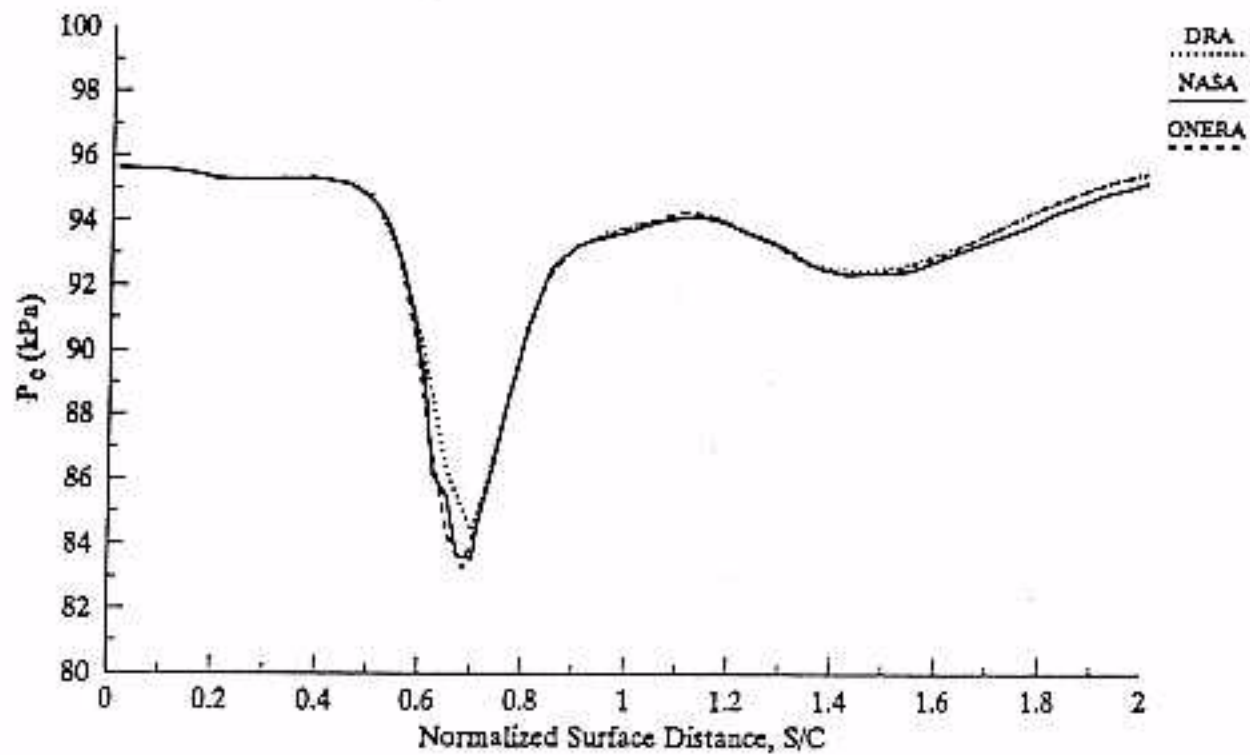


Figure 10 - 5 min Glaze Iced Cylinder
(Smooth Case)

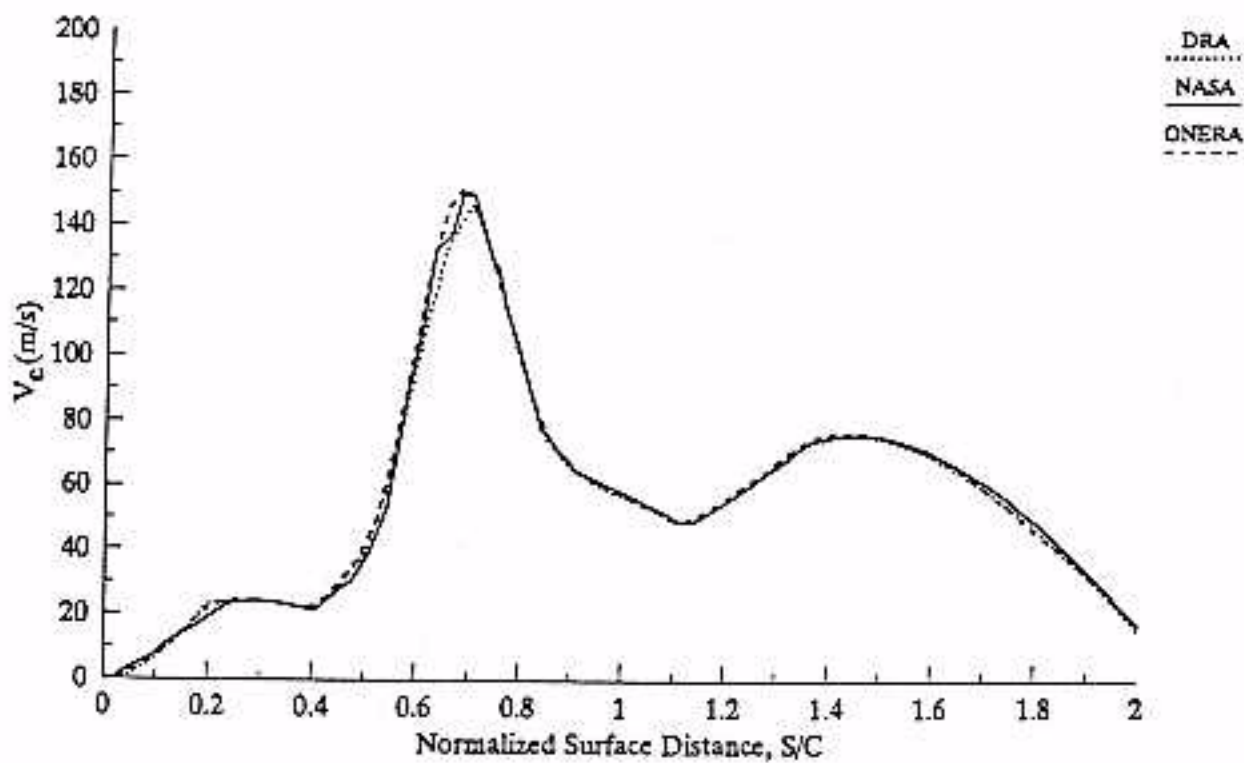


Figure 11 - 5 min Glaze Iced Cylinder
(Smooth Case)

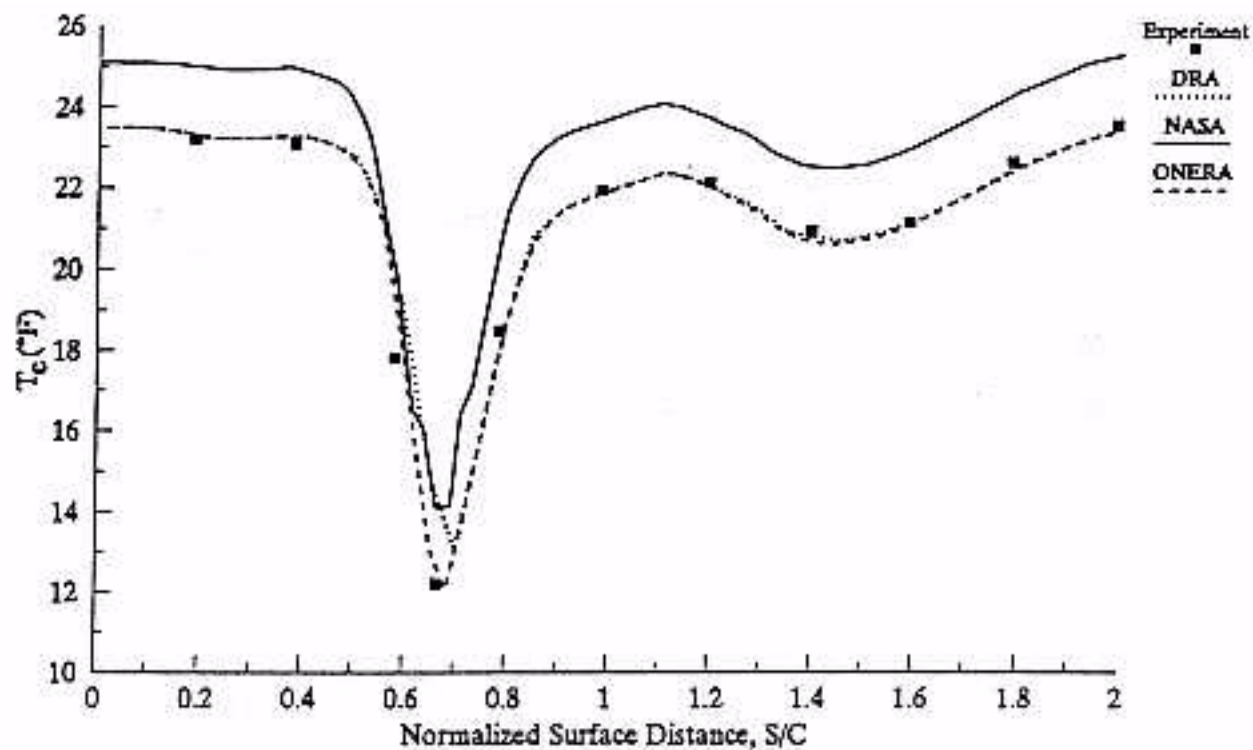


Figure 12 - 5 min Glaze Iced Cylinder
(Smooth Case)

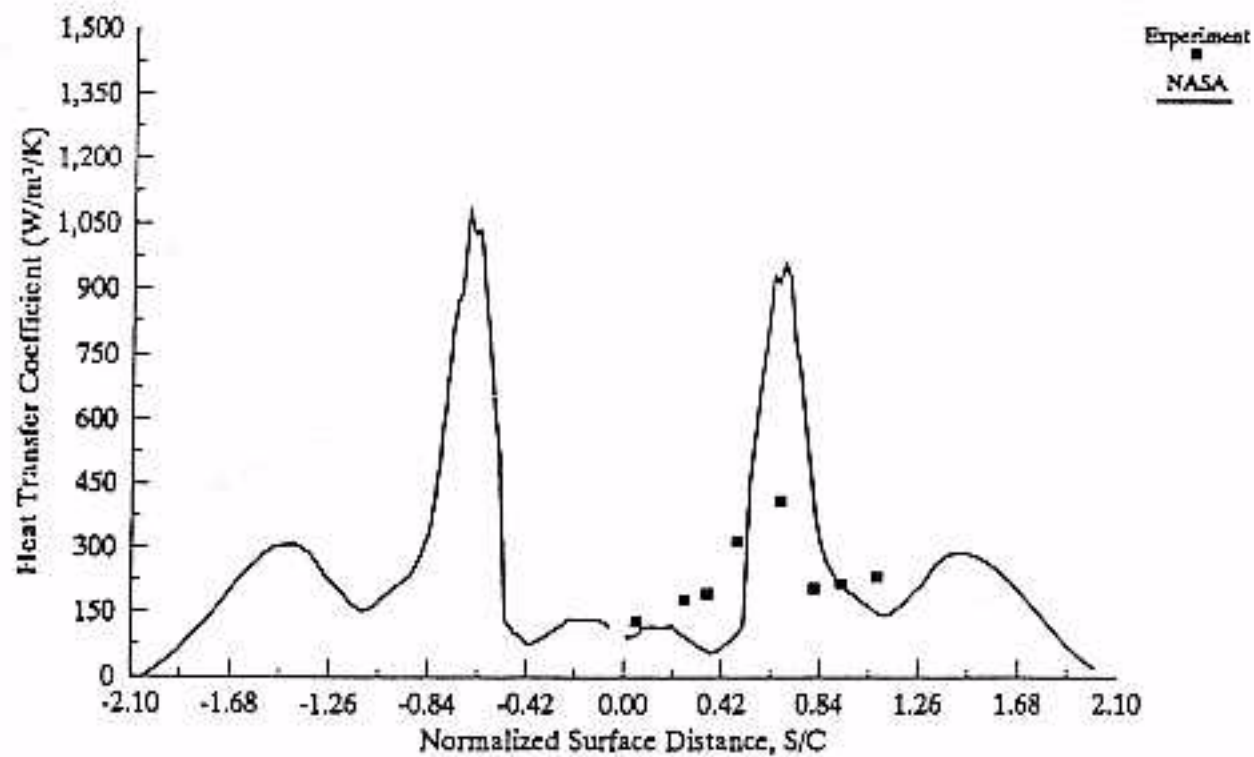


Figure 13 - 5 min Glaze Ice
(Rough Case)

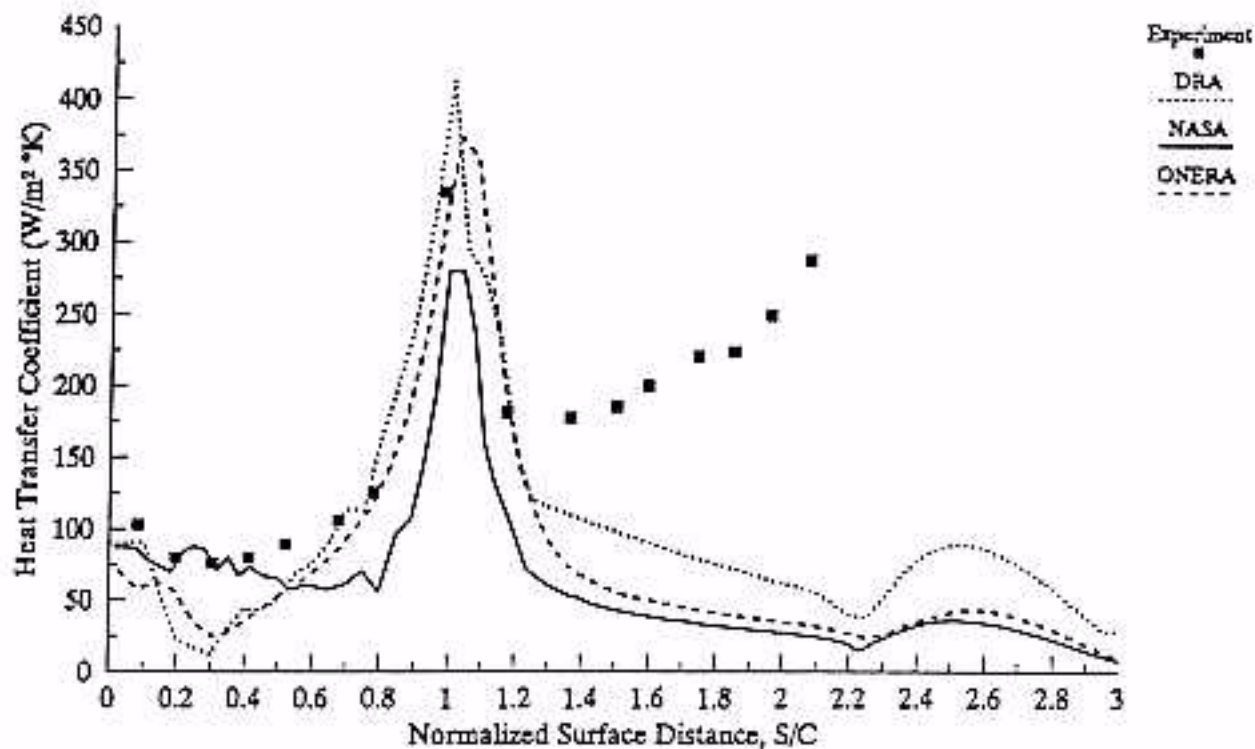


Figure 14 - 15 min Glaze Iced Cylinder
(Smooth Case)

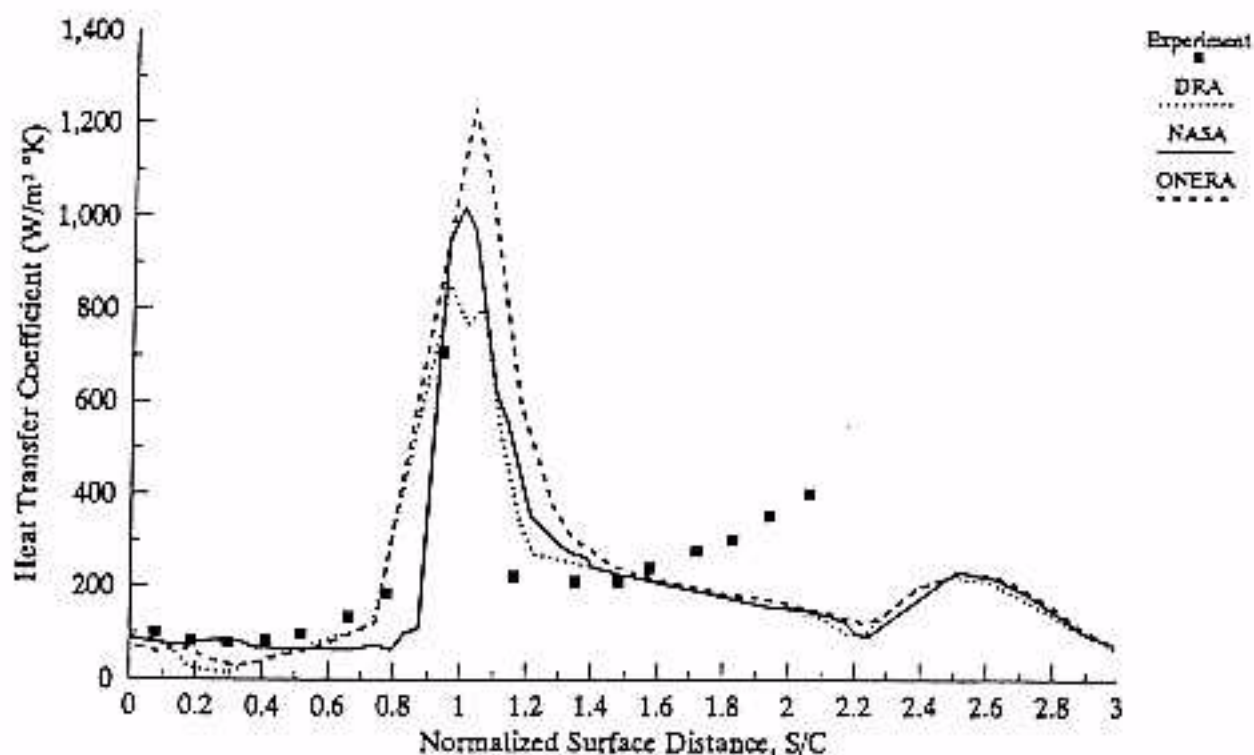


Figure 15 - 15 min Glaze Iced Cylinder
(Rough Case)

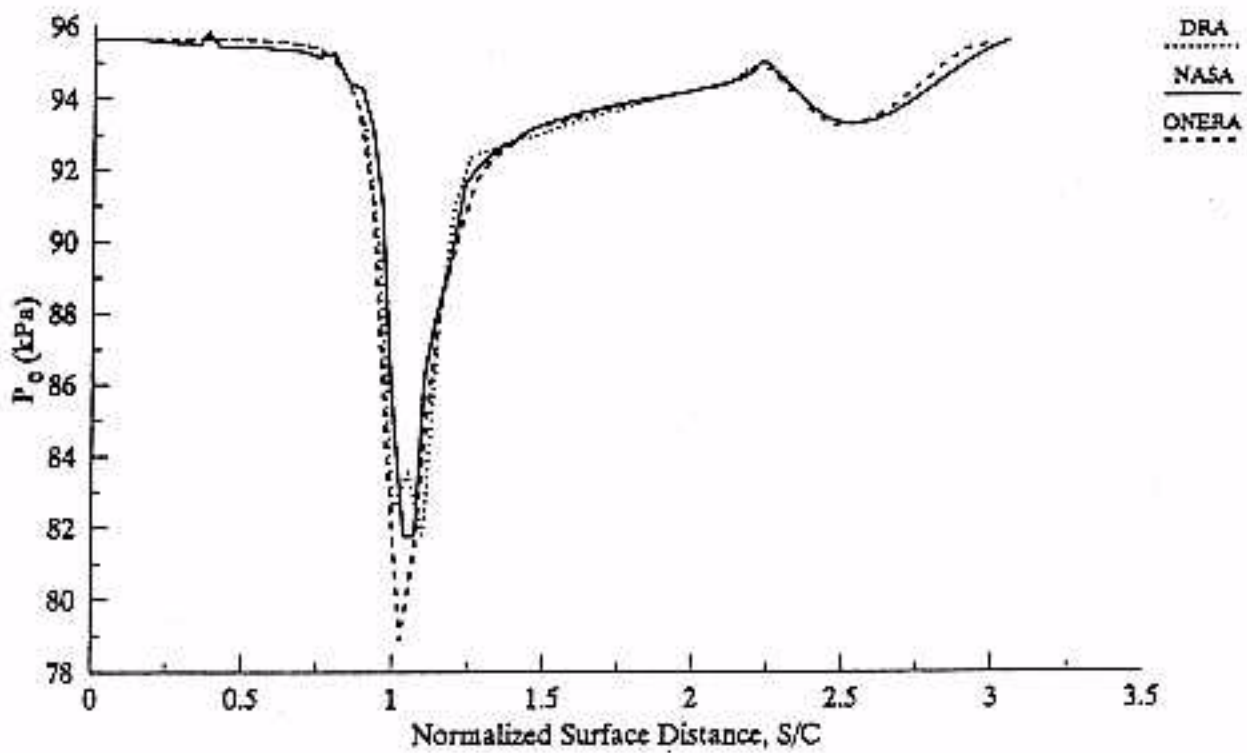


Figure 16 - 15 min Glaze Iced Cylinder
(Smooth Case)

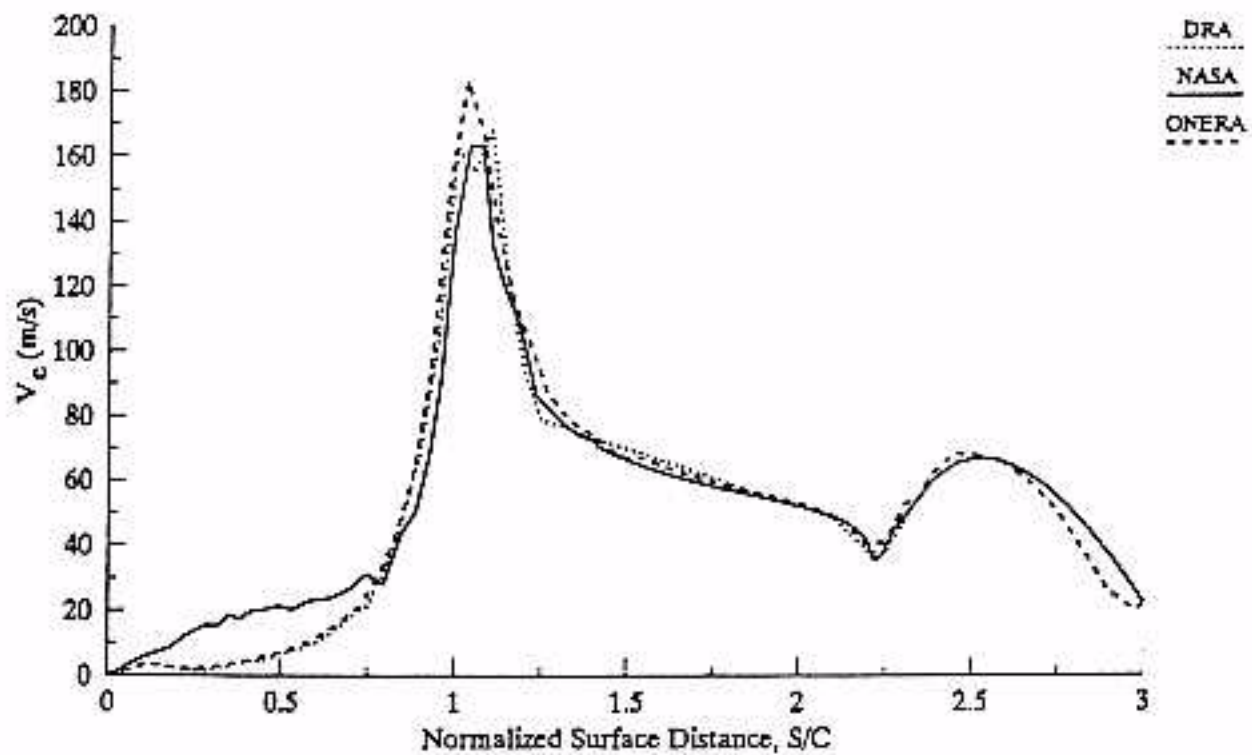


Figure 17 - 15 min Glaze Iced Cylinder
(Smooth Case)

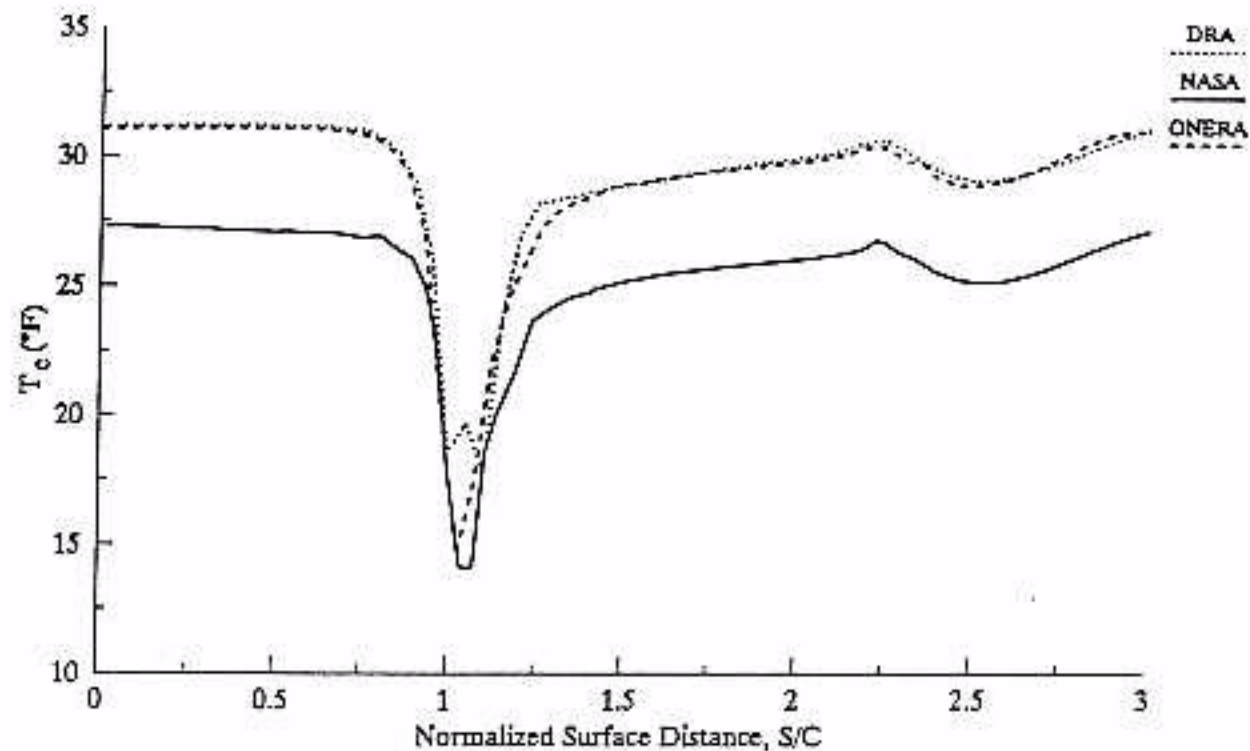


Figure 18 - 15 min Glaze Iced Cylinder
(Smooth Case)

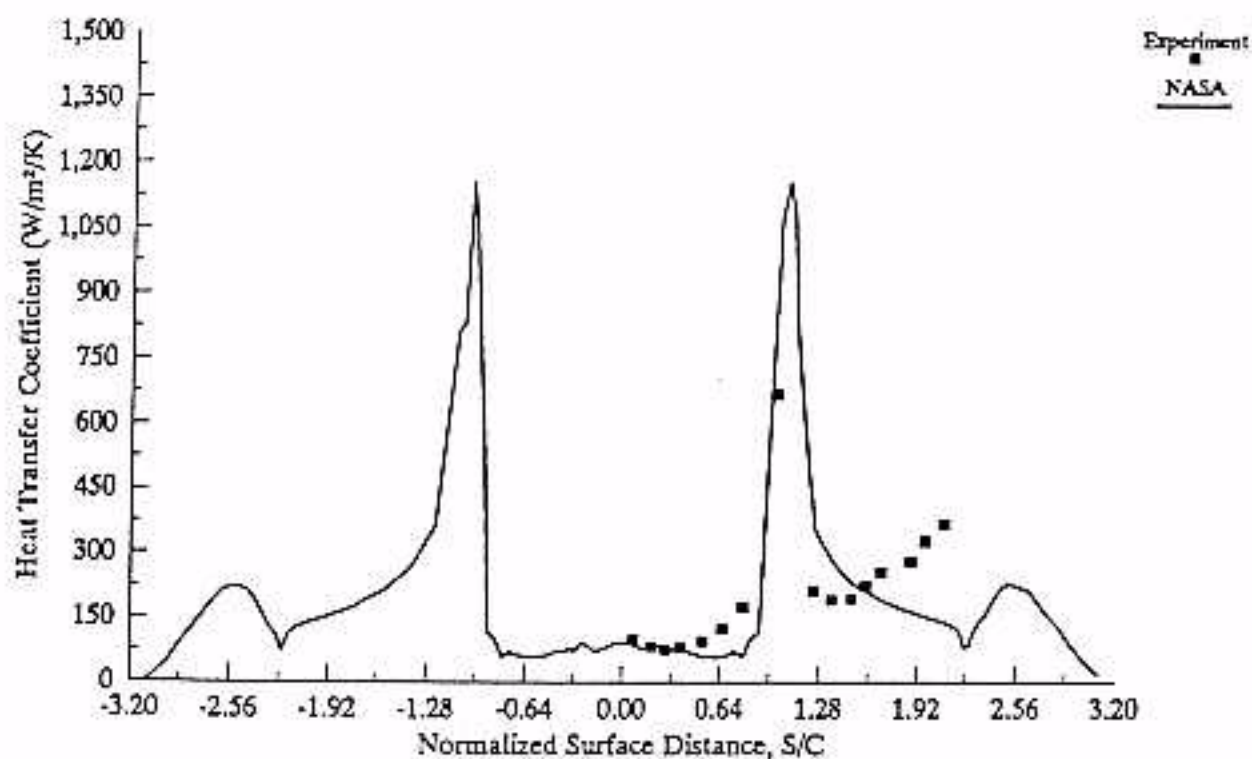


Figure 19 - 15 min Glaze Ice
(Rough Case)

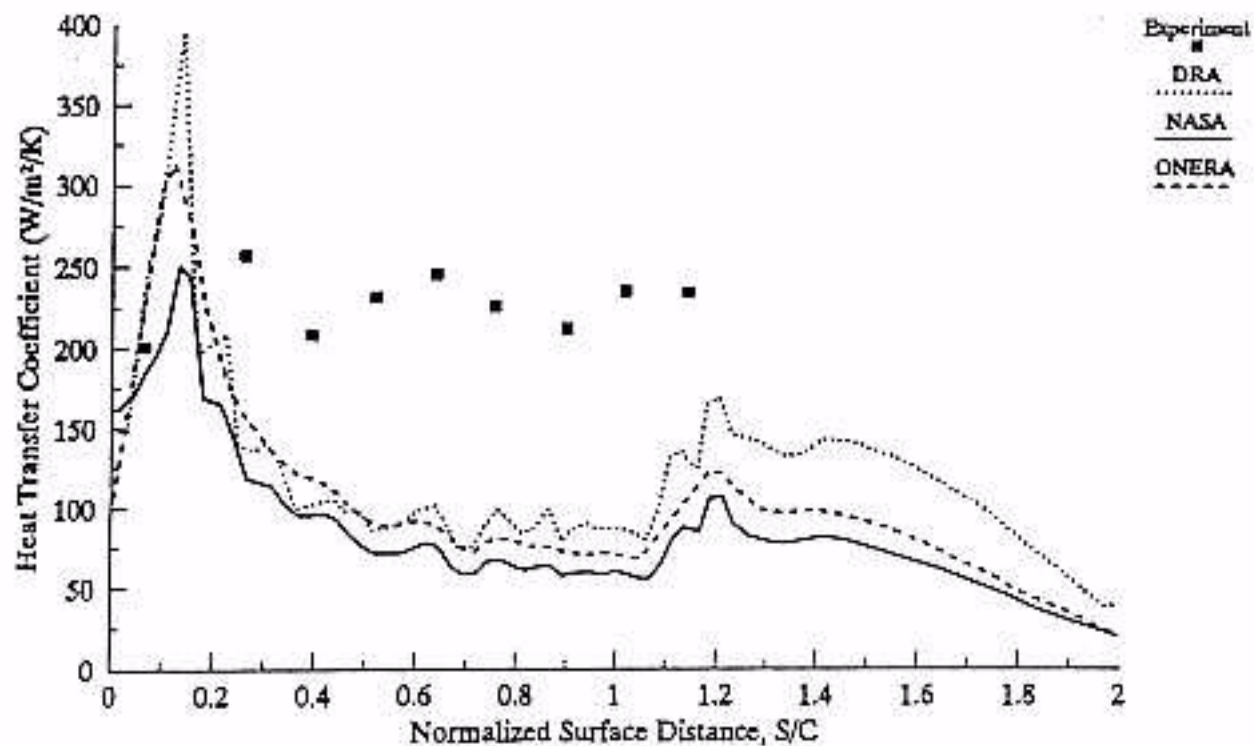


Figure 20 - 15 min Rime Iced Cylinder
(Smooth Case)

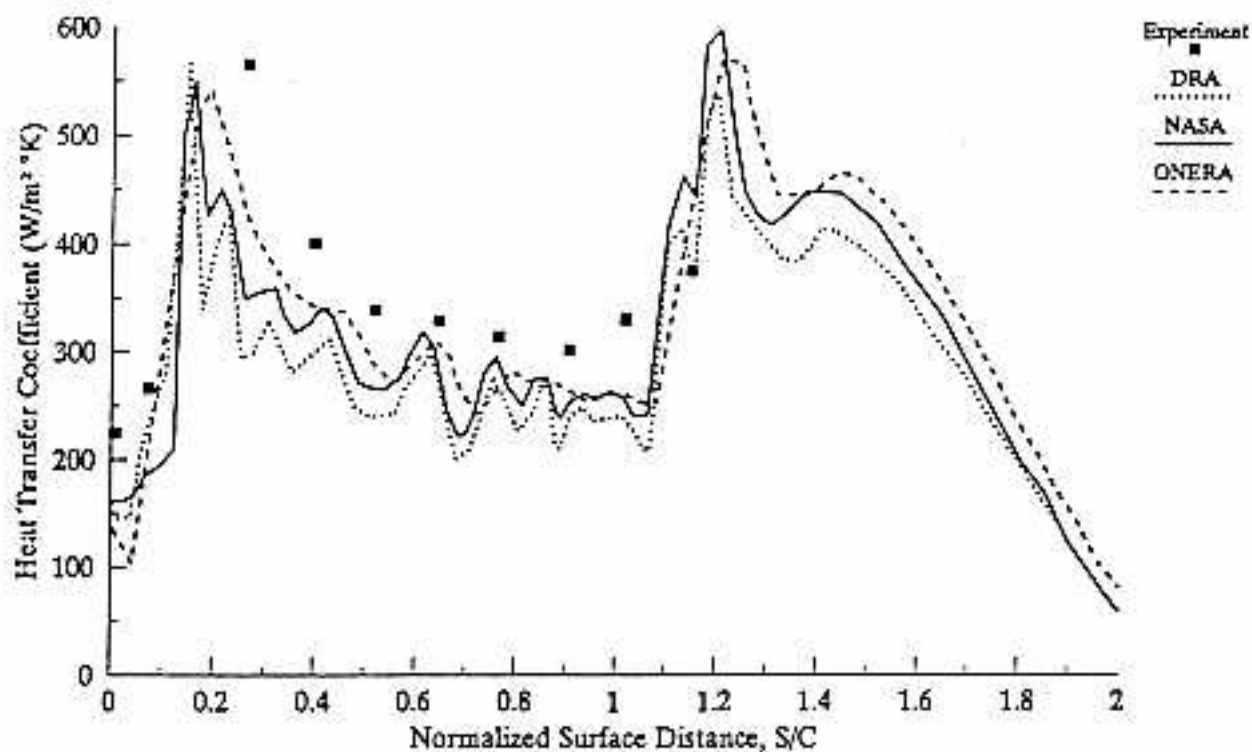


Figure 21 - 15 min Glaze Iced Cylinder
(Rough Case)

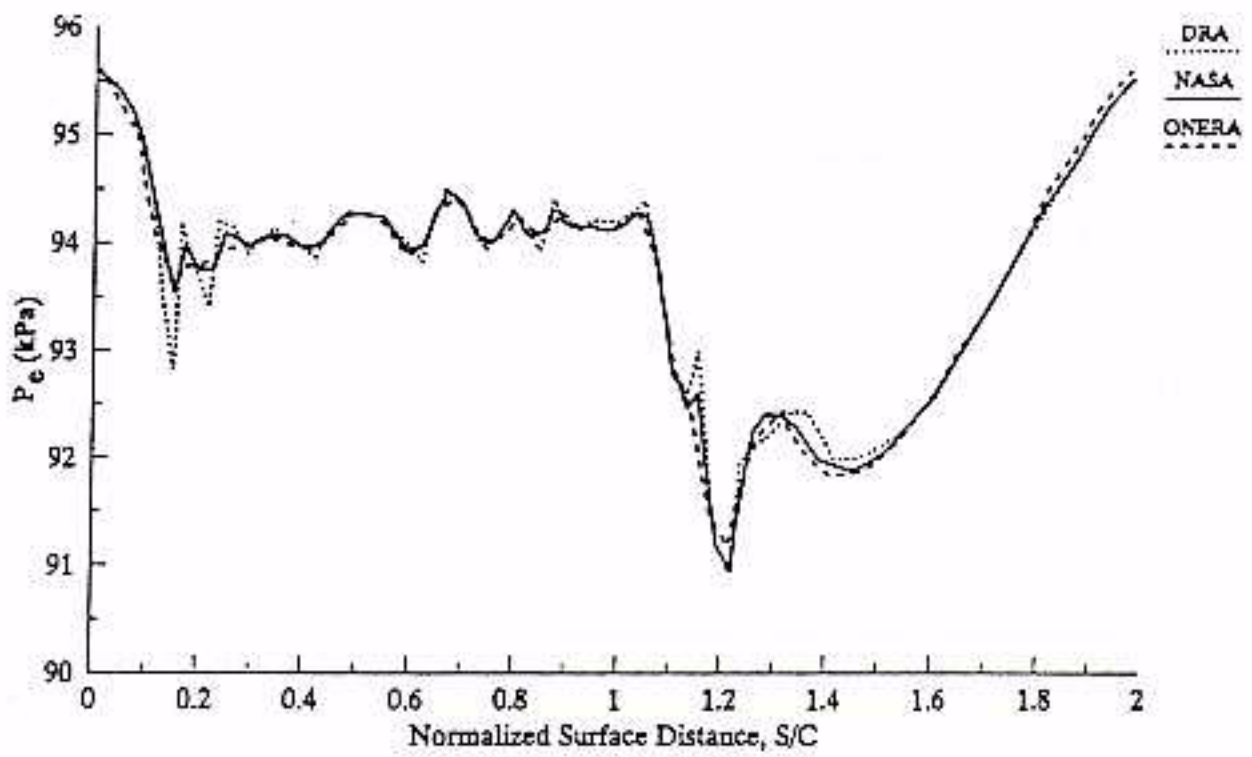


Figure 22 - 15 min Rime Iced Cylinder
(Smooth Case)

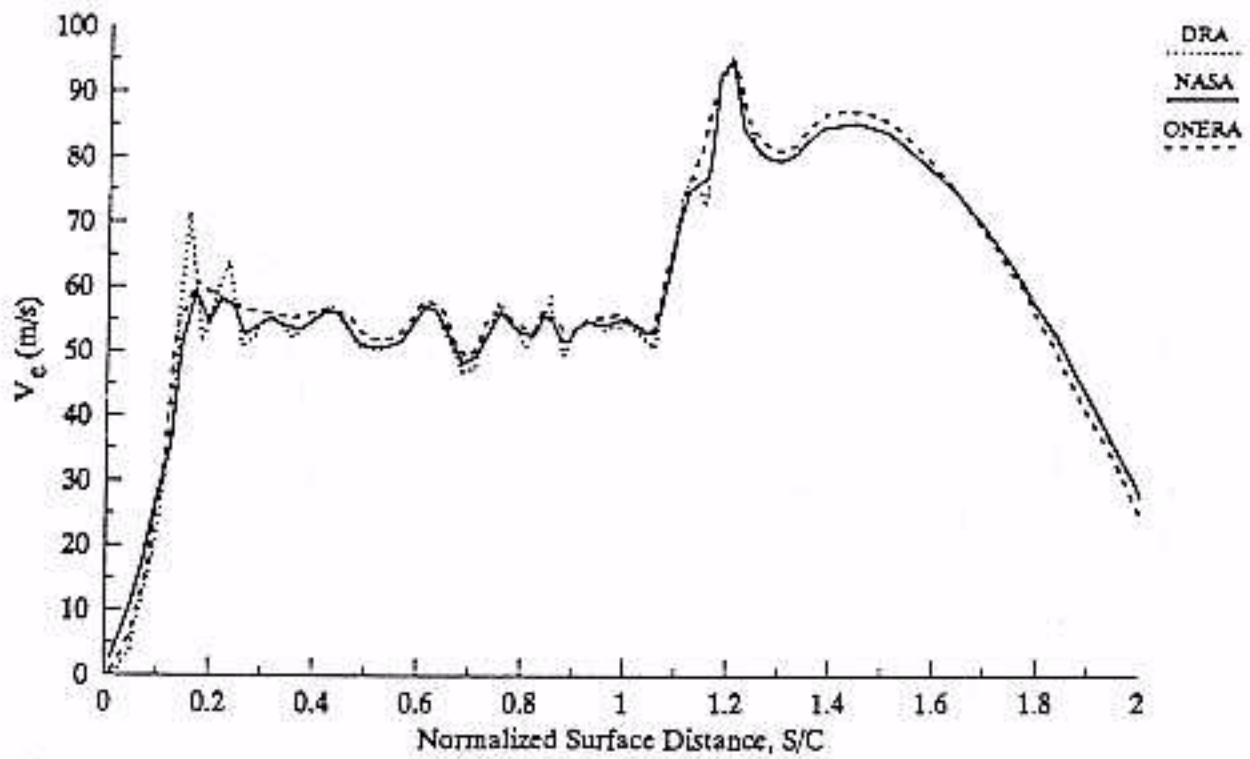


Figure 23 - 15 min Rime Iced Cylinder
(Smooth Case)

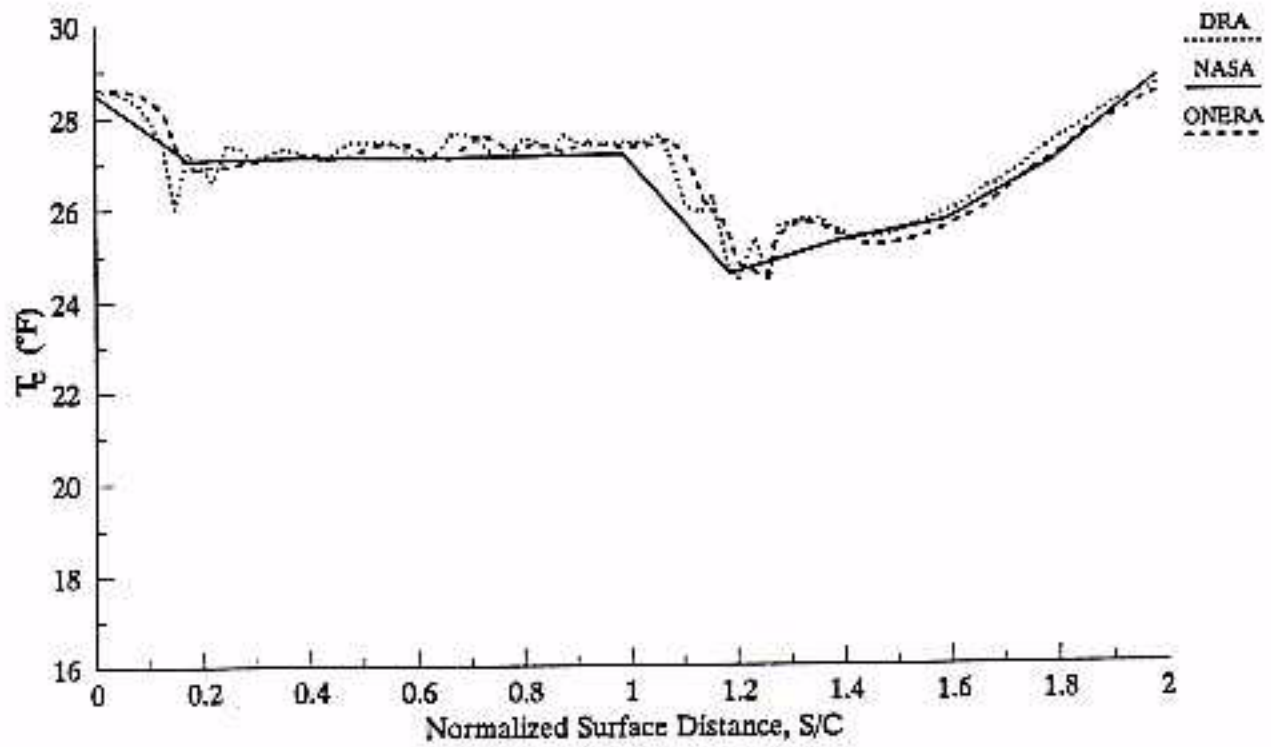


Figure 24 - 15 min Rime Iced Cylinder
(Smooth Case)

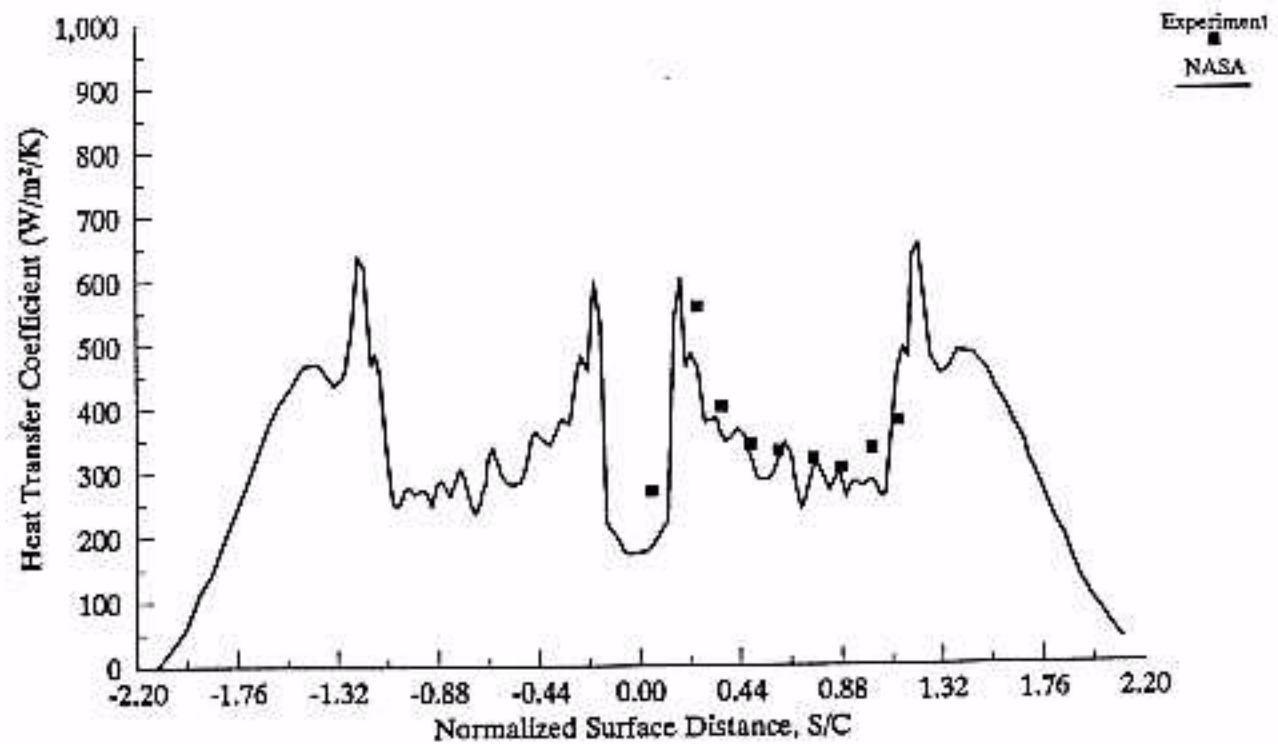


Figure 25 - 15 min Rime Ice
(Rough Case)

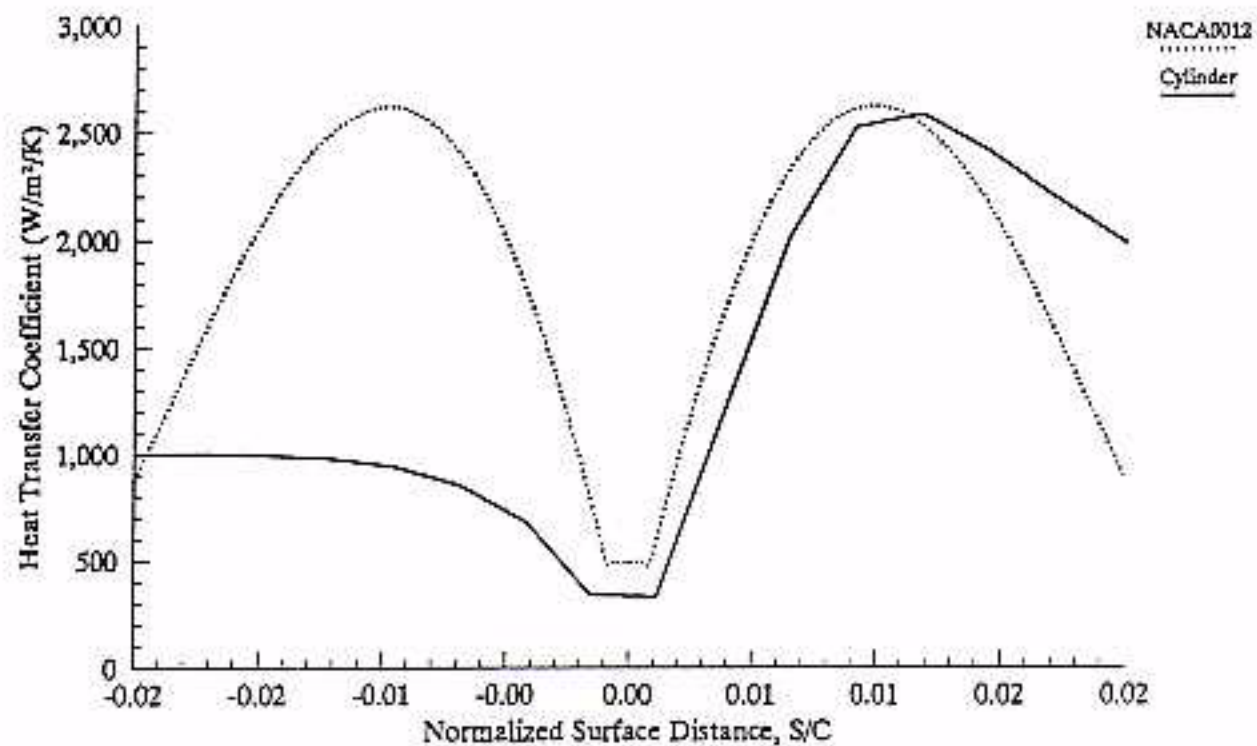


Figure 26 - Comparison of Heat Transfer Coefficient for a NACA0012 at $\alpha = 4^\circ$ and a Cylinder

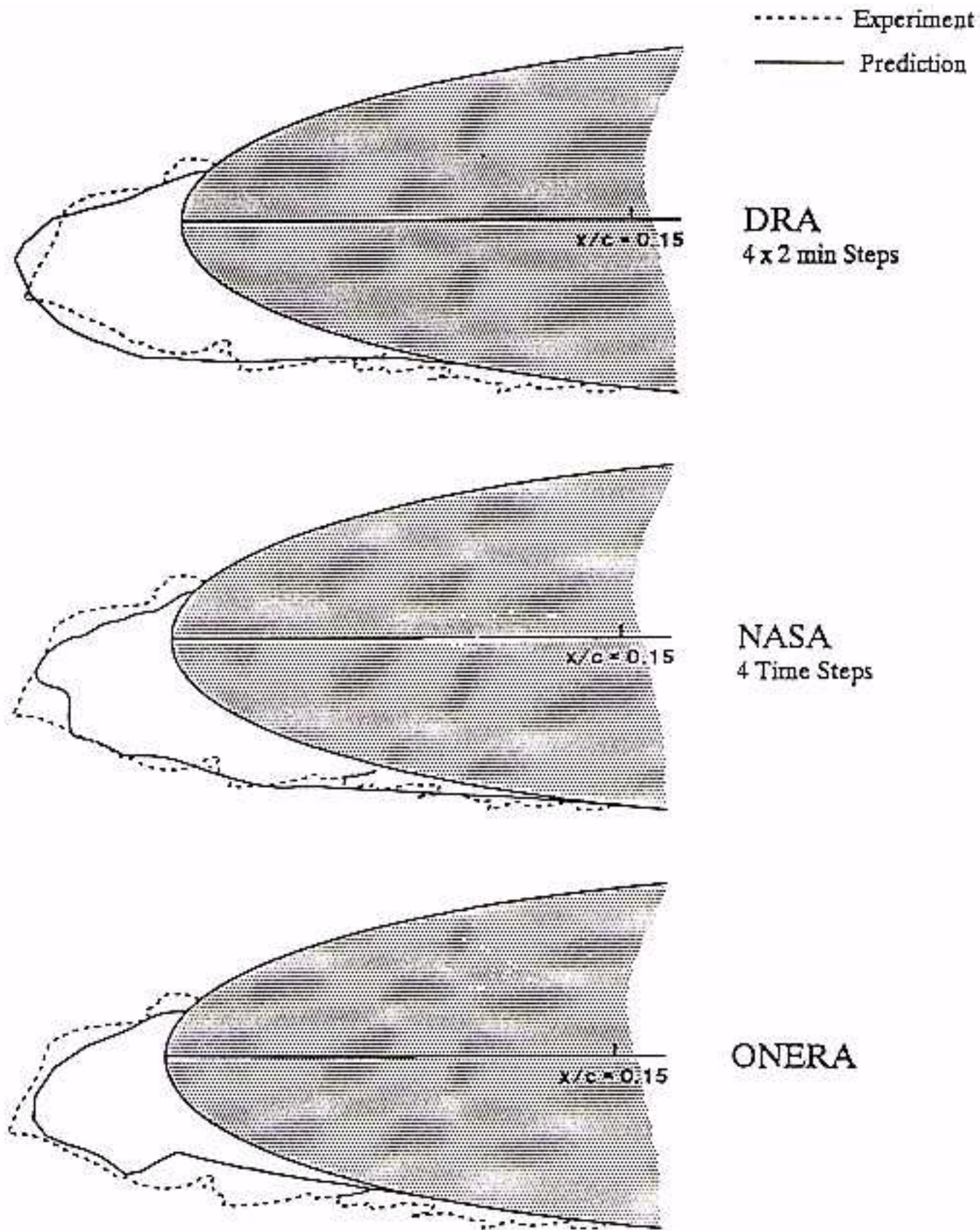


Figure 27 - Comparison of ice shape predictions for NASA cases.

NACA0012, Chord = 0.53, $\alpha = 4.0$, $V_\infty = 58.1$, $T_s = -27.8^\circ\text{C}$, $LWC = 1.3$, $MVD = 20.0\mu$, $\tau = 480.0$

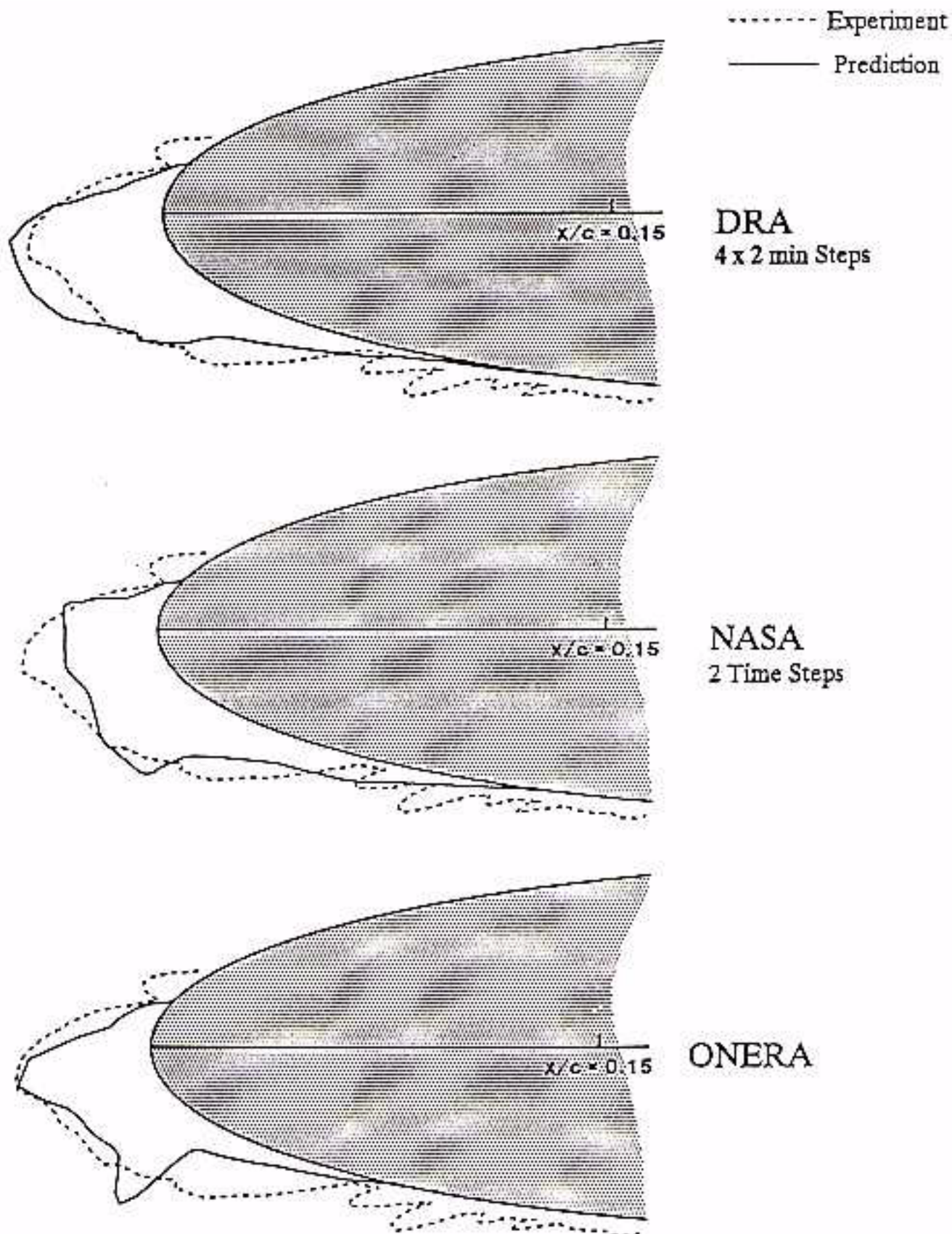


Figure 28 - Comparison of ice shape predictions for NASA cases.

NACA0012, Chord = 0.53, $\alpha = 4.0$, $V_\infty = 58.1$, $T_s = -19.8^\circ\text{C}$, LWC = 1.3, MVD = 20.0μ , $r = 480.0$

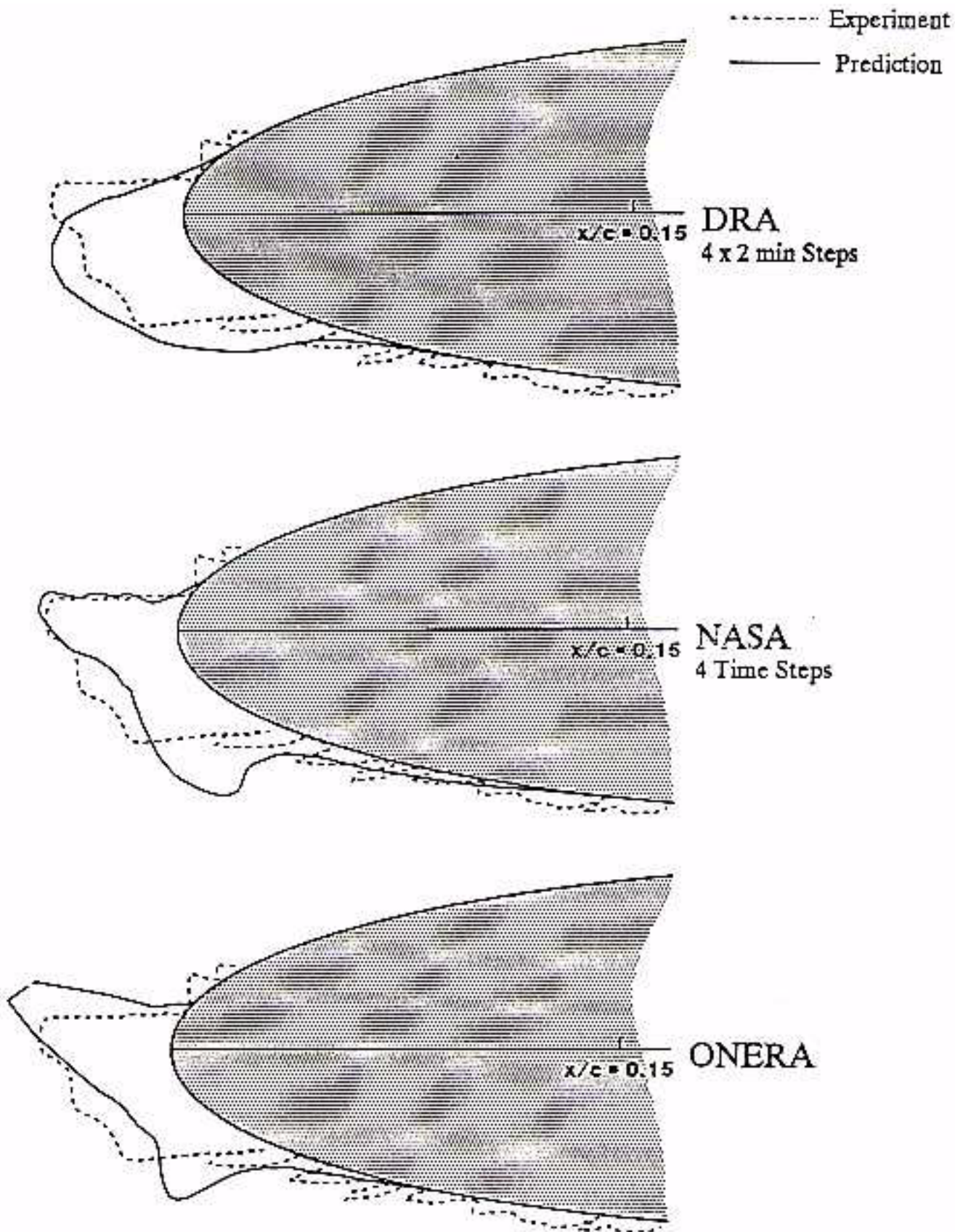


Figure 29 - Comparison of ice shape predictions for NASA cases.

NACA0012, Chord = 0.53, $\alpha = 4.0$, $V_\infty = 58.1$, $T_s = -13.9^\circ\text{C}$, LWC = 1.3, MVD = 20.0μ , $\tau = 480.0$

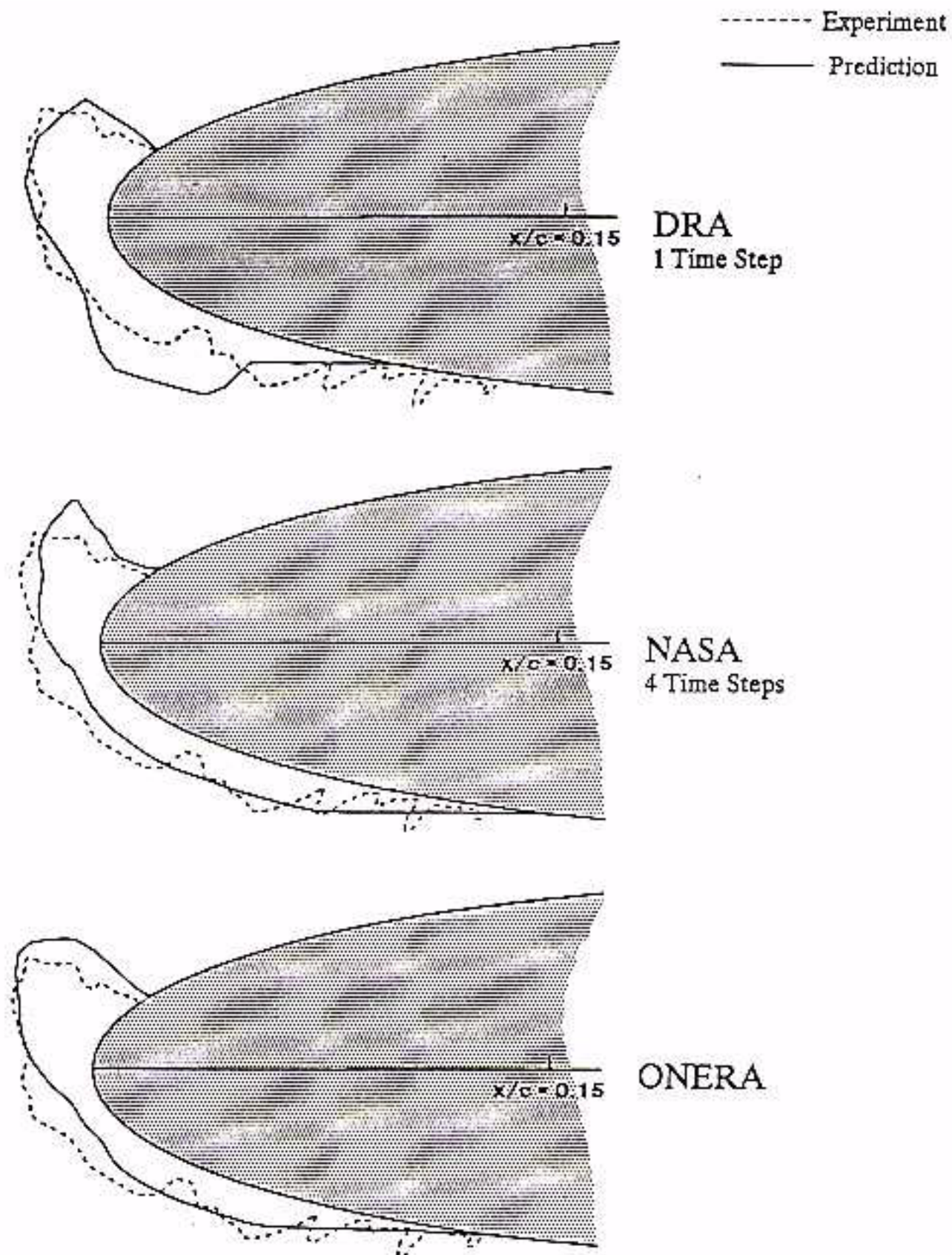


Figure 30 - Comparison of ice shape predictions for NASA cases.

NACA0012, Chord = 0.53, $\alpha = 4.0$, $V_\infty = 58.1$, $T_s = -6.7^\circ\text{C}$, $\text{LWC} = 1.3$, $\text{MVD} = 20.0\mu$, $\tau = 480.0$

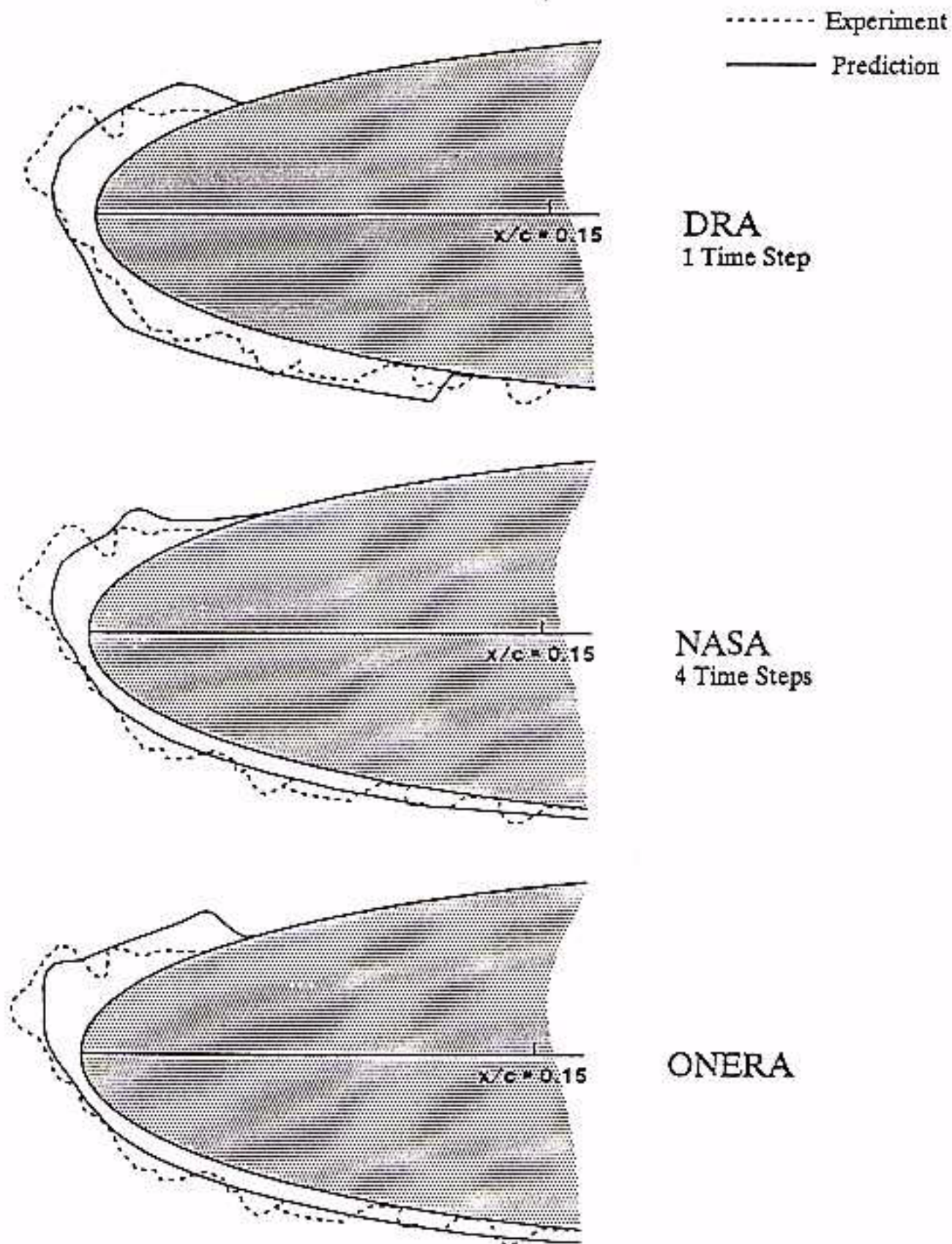


Figure 31 - Comparison of ice shape predictions for NASA cases.

NACA0012, Chord = 0.53, $\alpha = 4.0$, $V_\infty = 58.1$, $T_s = -3.9^\circ\text{C}$, $\text{LWC} = 1.3$, $\text{MVD} = 20.0\mu$, $\tau = 480.0$

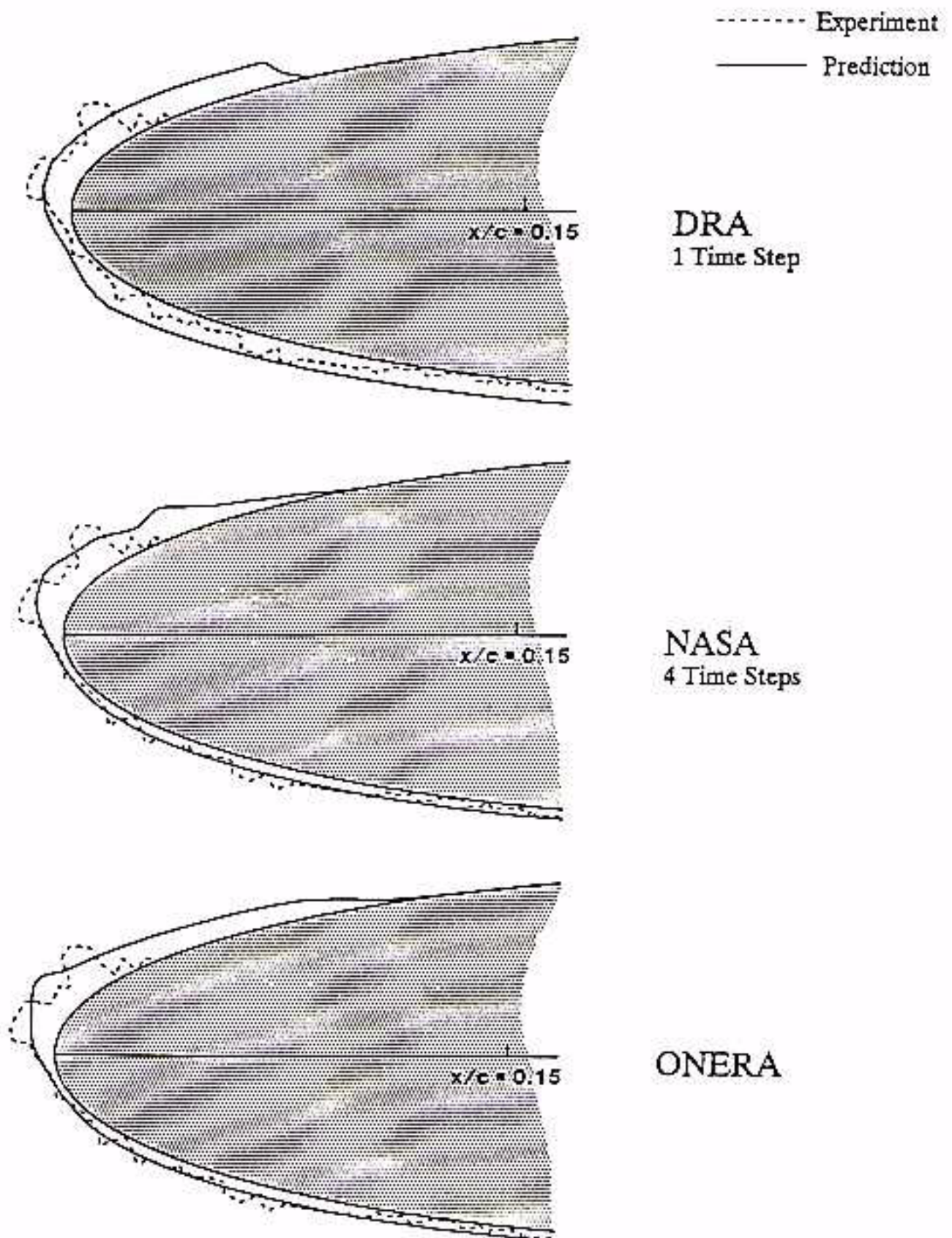


Figure 32 - Comparison of ice shape predictions for NASA cases.

NACA0012, Chord = 0.53, $\alpha = 4.0$, $V_\infty = 58.1$, $T_s = -2.8^\circ\text{C}$, $\text{LWC} = 1.3$, $\text{MVD} = 20.0\mu$, $\tau = 480.0$

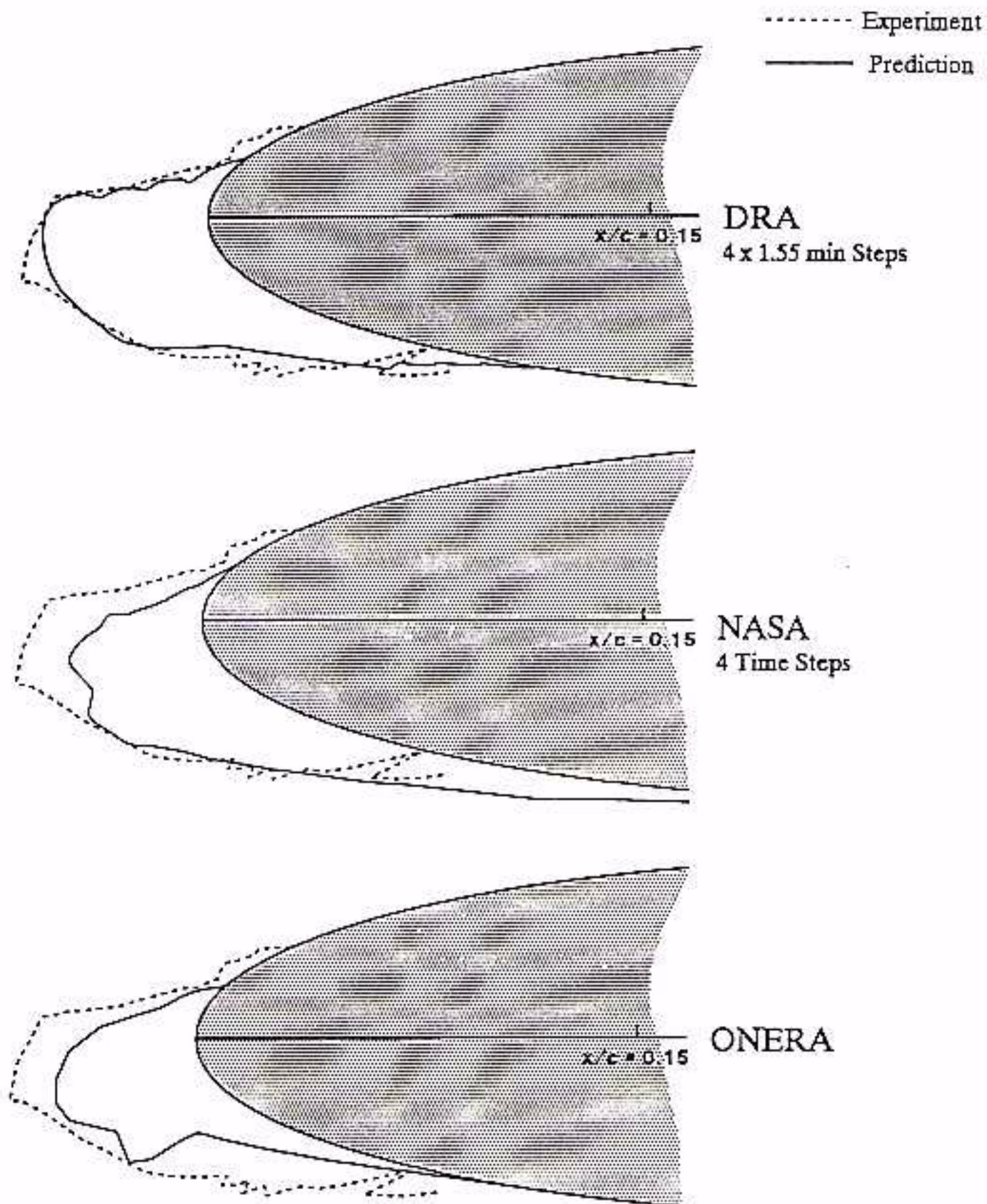


Figure 33 - Comparison of ice shape predictions for NASA cases.

NACA0012, Chord = 0.53, $\alpha = 4.0$, $V_\infty = 93.9$, $T_s = -30.5^\circ\text{C}$, LWC = 1.05, MVD = 20.0 μ , $\tau = 372.0$

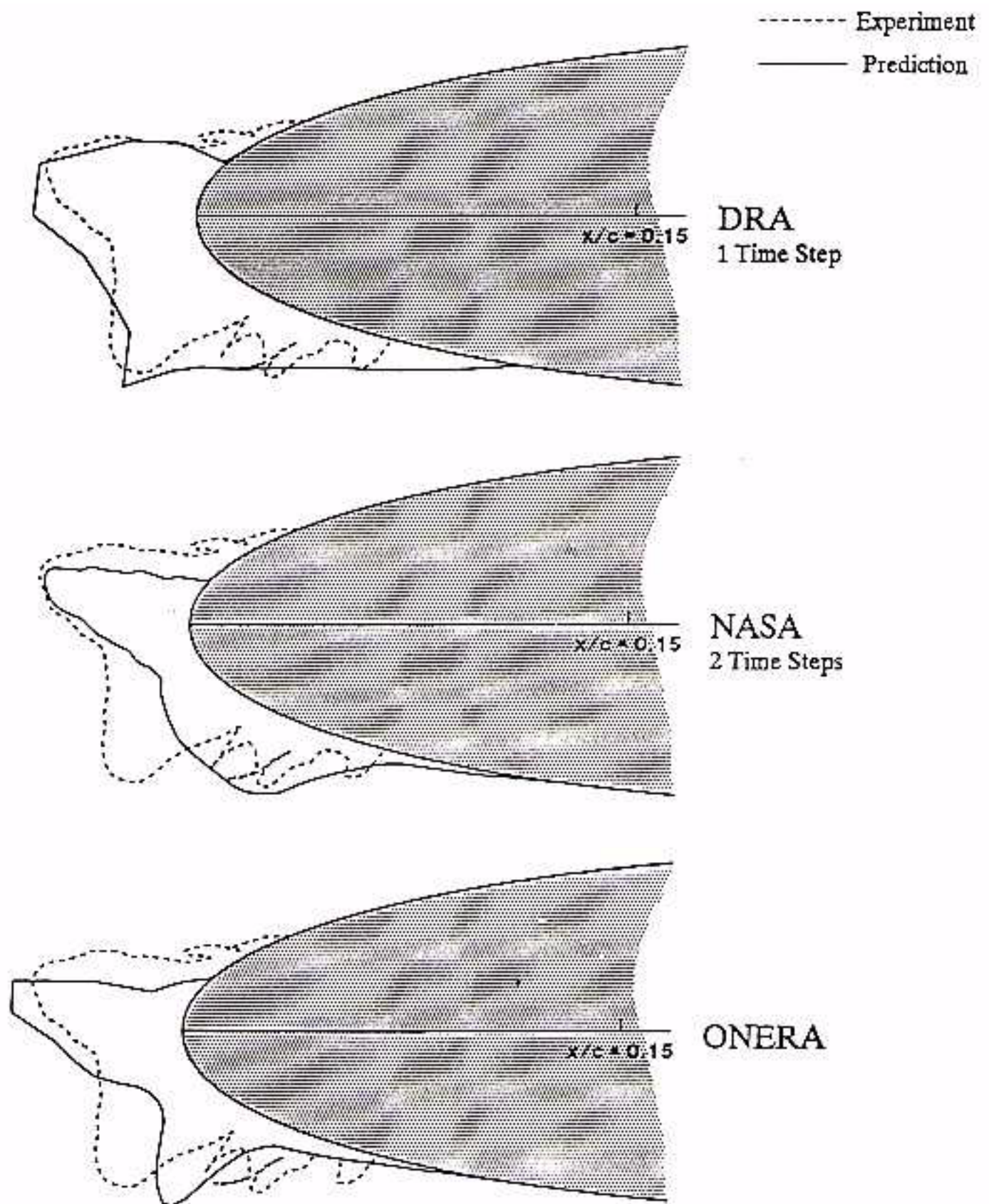


Figure 34 - Comparison of ice shape predictions for NASA cases.

NACA0012, Chord = 0.53, $\alpha = 4.0$, $V_\infty = 93.9$, $T_s = -16.6^\circ\text{C}$, LWC = 1.05, MVD = 20.0 μm , $\tau = 372.0$

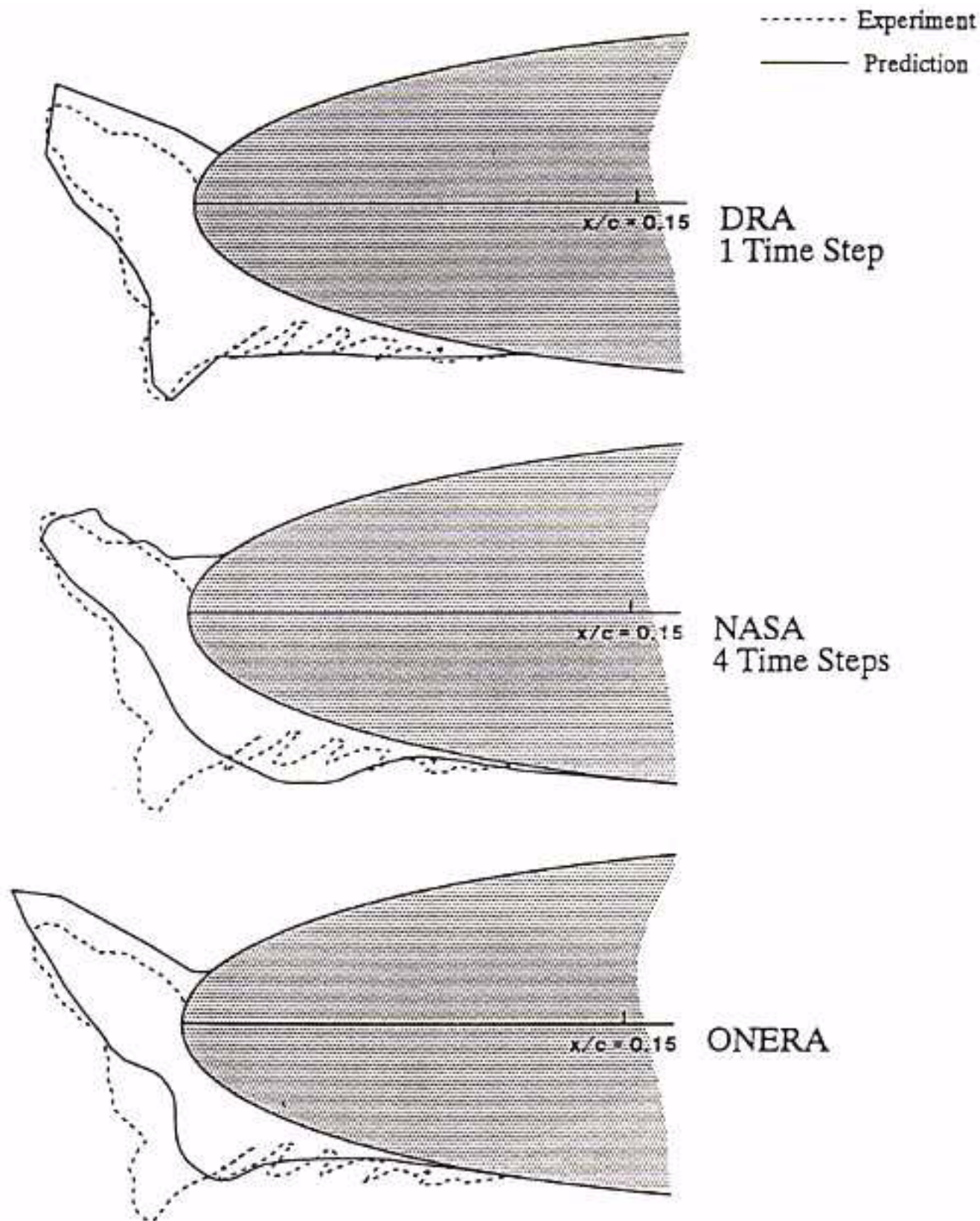


Figure 35 - Comparison of ice shape predictions for NASA cases.

NACA0012, Chord = 0.53, $\alpha = 4.0$, $V_\infty = 93.9$, $T_s = -12.2^\circ\text{C}$, $\text{LWC} = 1.05$, $\text{MVD} = 20.0\mu$, $\tau = 372.0$

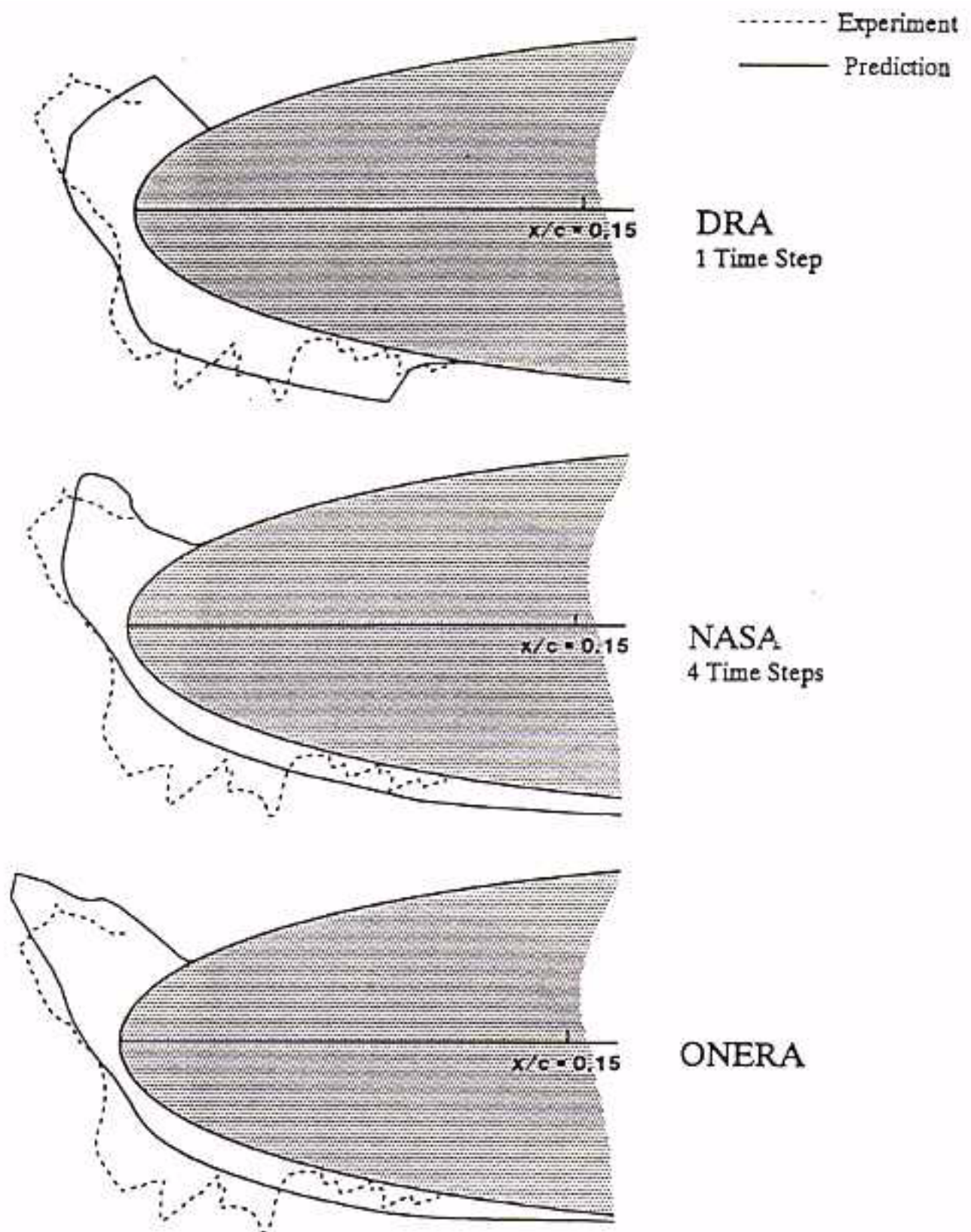


Figure 36A - Comparison of ice shape predictions for NASA cases.

NACA0012, Chord = 0.53, $\alpha = 4.0$, $V_\infty = 93.9$, $T_s = -6.6^\circ\text{C}$, LWC = 1.05, MVD = 20.0μ , $\tau = 480.0$

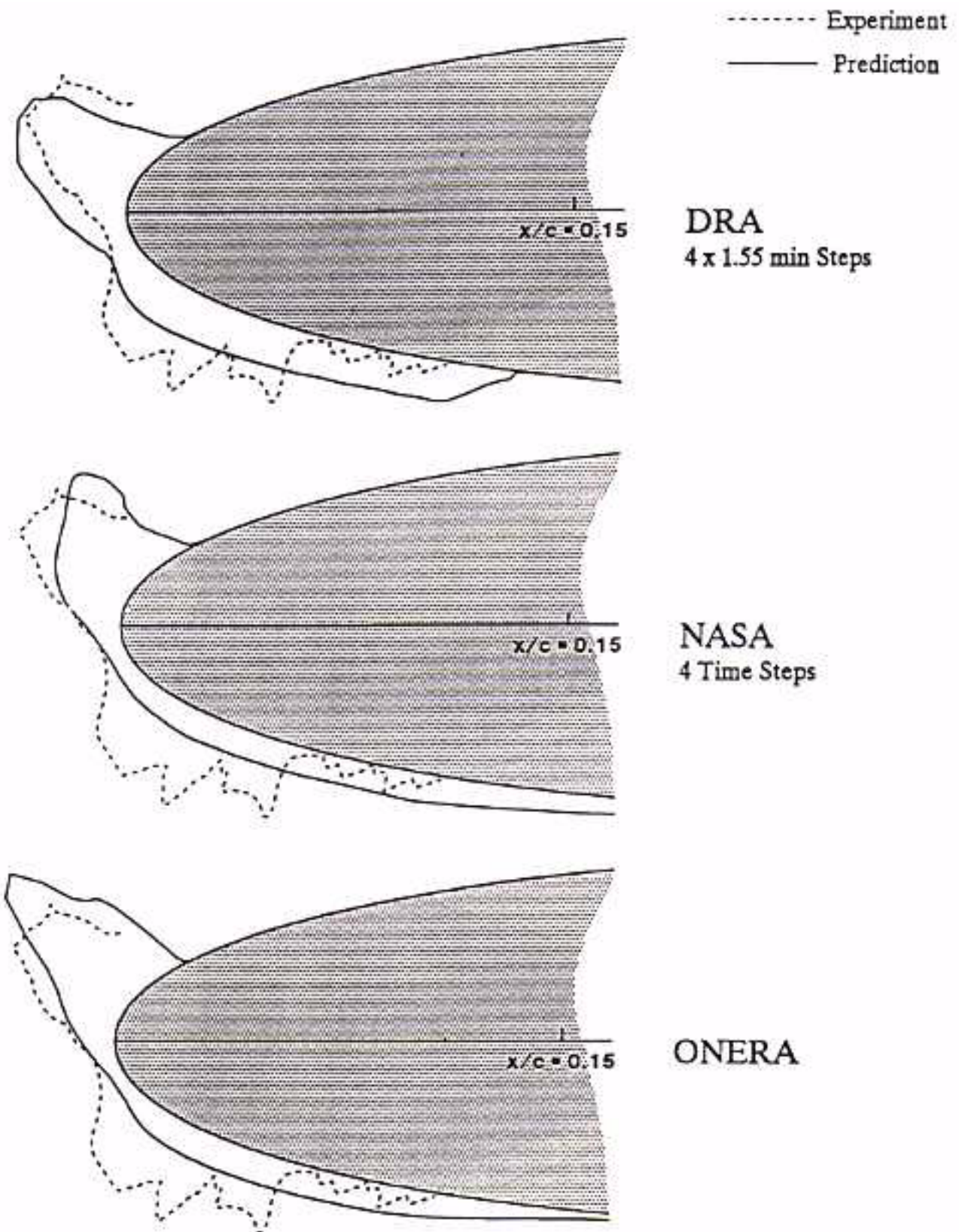


Figure 36B - Comparison of ice shape predictions for NASA cases.

NACA0012, Chord = 0.53, $\alpha = 4.0$, $V_\infty = 93.9$, $T_s = -6.6^\circ\text{C}$, $LWC = 1.05$ MVD = 20.0μ , $\tau = 480.0$

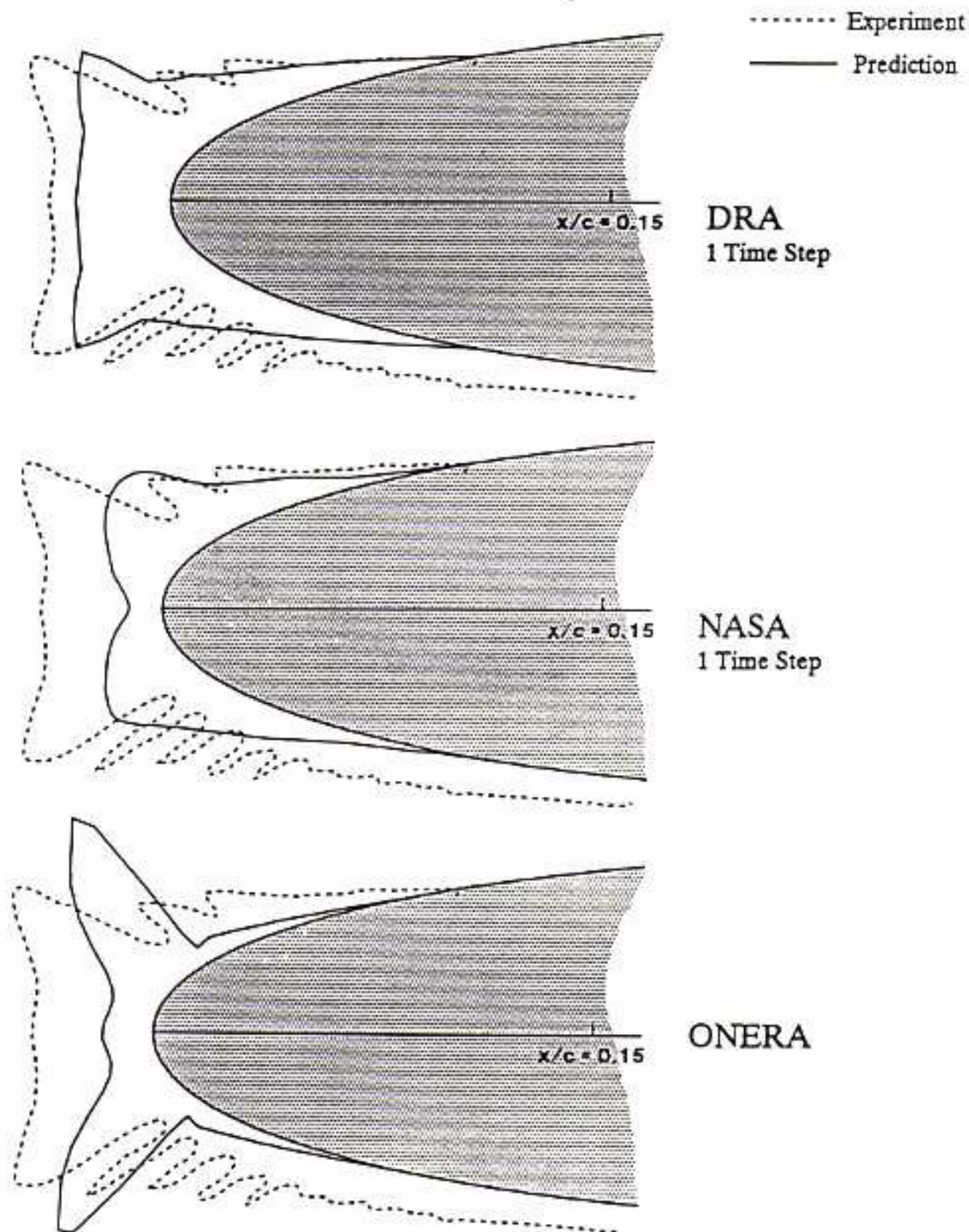


Figure 37 - Comparison of ice shape predictions for DRA cases.

NACA0012, Chord = 0.53, $\alpha = 0.0$, $V_\infty = 130.5$, $T_s = -12.3^\circ\text{C}$, LWC = 0.5, MVD = 20.0μ , $\tau = 480.0$

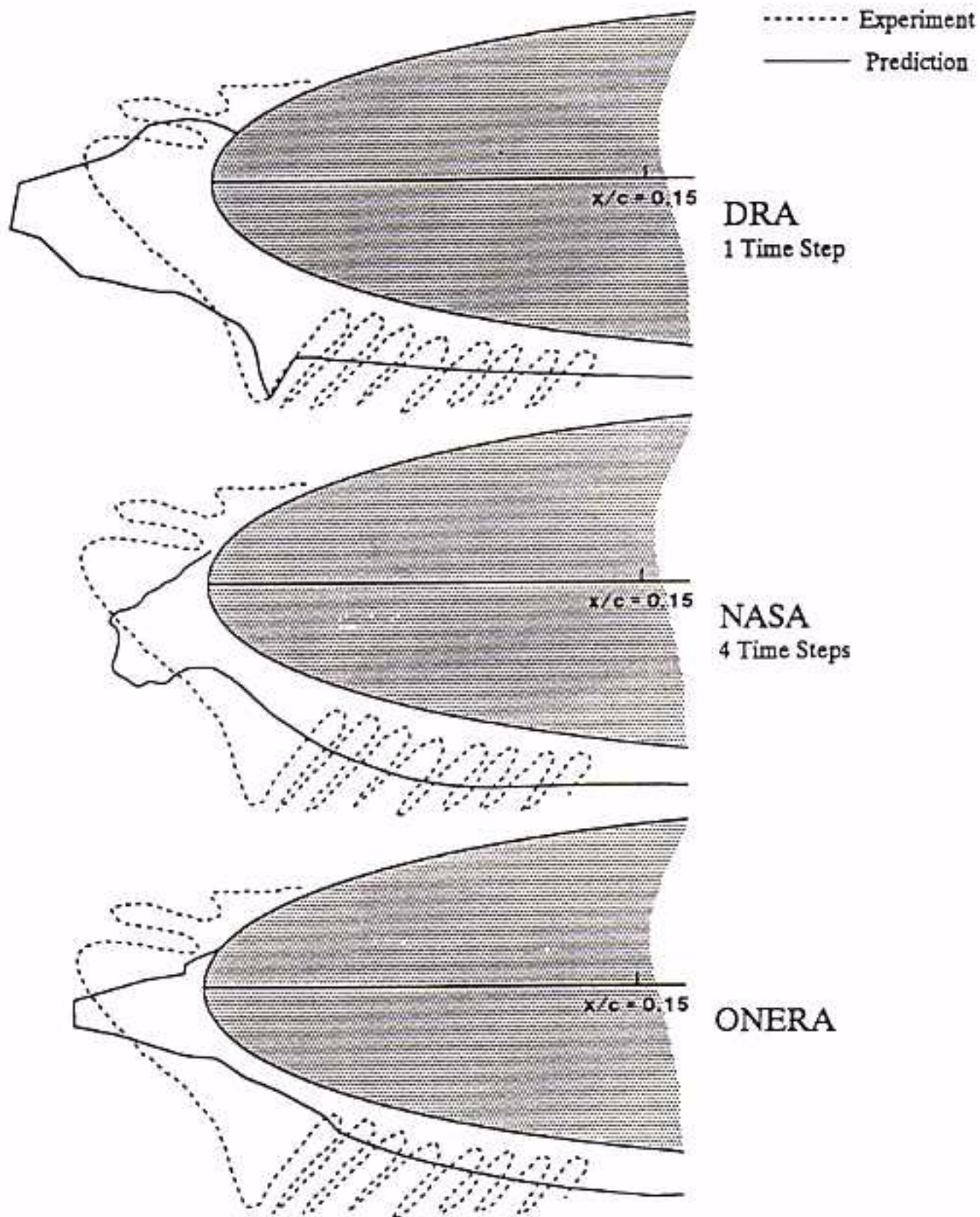


Figure 38A - Comparison of ice shape predictions for DRA cases.

NACA0012, Chord = 0.53, $\alpha = 8.5$, $V_\infty = 130.5$, $T_s = -12.3^\circ\text{C}$, LWC = 0.5, MVD = 17.5μ , $\tau = 120.0$

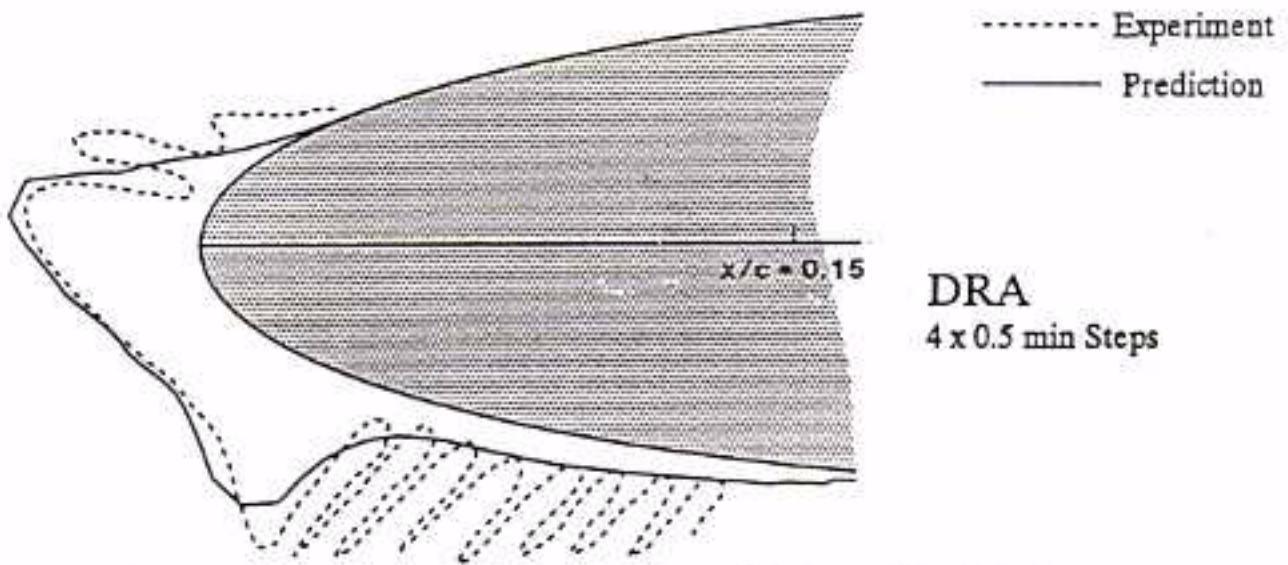


Figure 38B - Comparison of ice shape predictions for DRA cases.

NACA0012, Chord = 0.53, $\alpha = 2.0$, $V_\infty = 130.5$, $T_s = -12.3^\circ\text{C}$, $LWC = 0.5$, $MVD = 17.5\mu$, $\tau = 120.0$

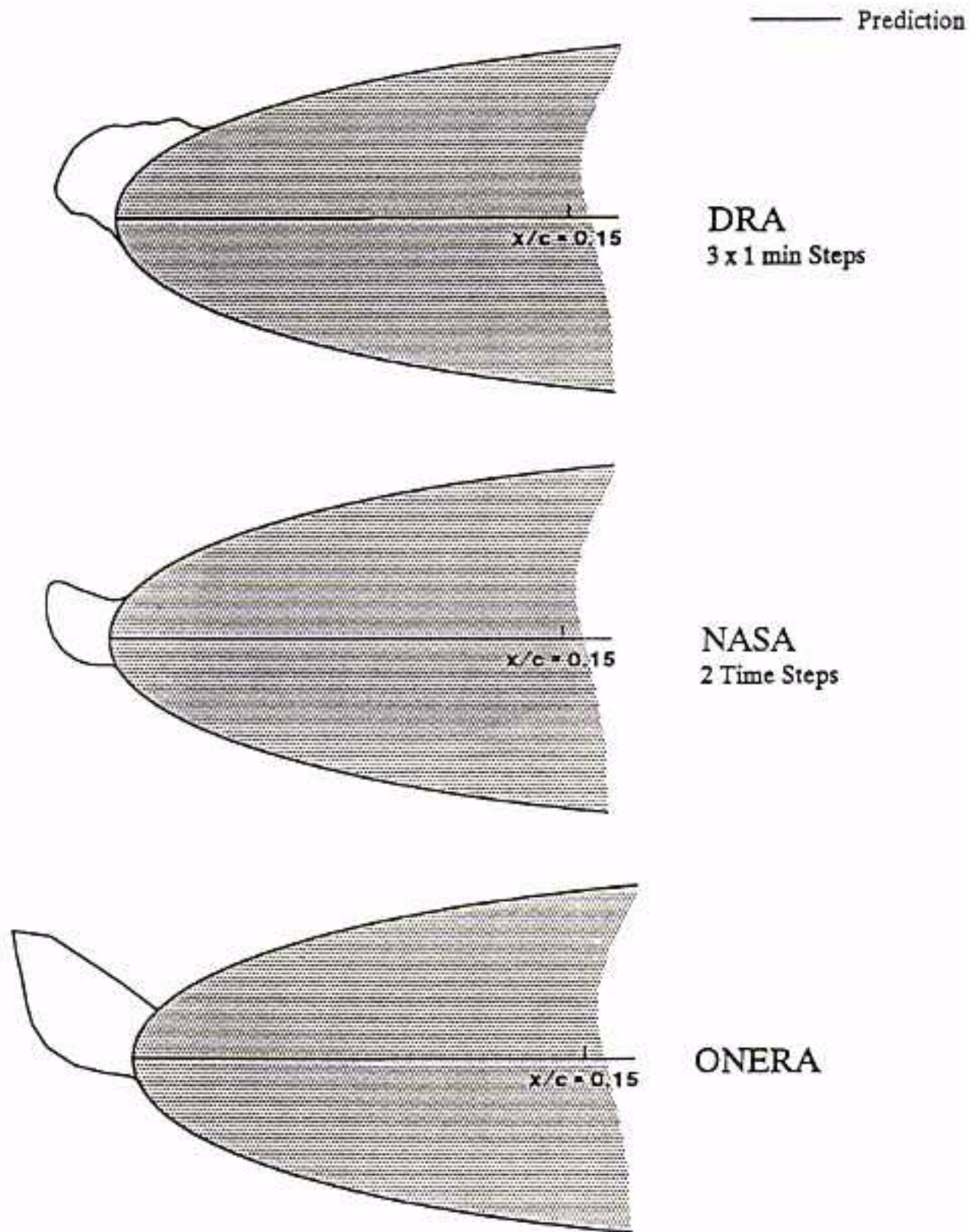


Figure 39 - Comparison of ice shape predictions for DRA cases.

NACA0012, $C_{\text{bord}} = 0.53$, $\alpha = 8.0$, $V_{\infty} = 131.5$, $T_s = -3.9^{\circ}\text{C}$, $\text{LWC} = 0.6$, $\text{MVD} = 20.0\mu\text{m}$, $\tau = 180.0$

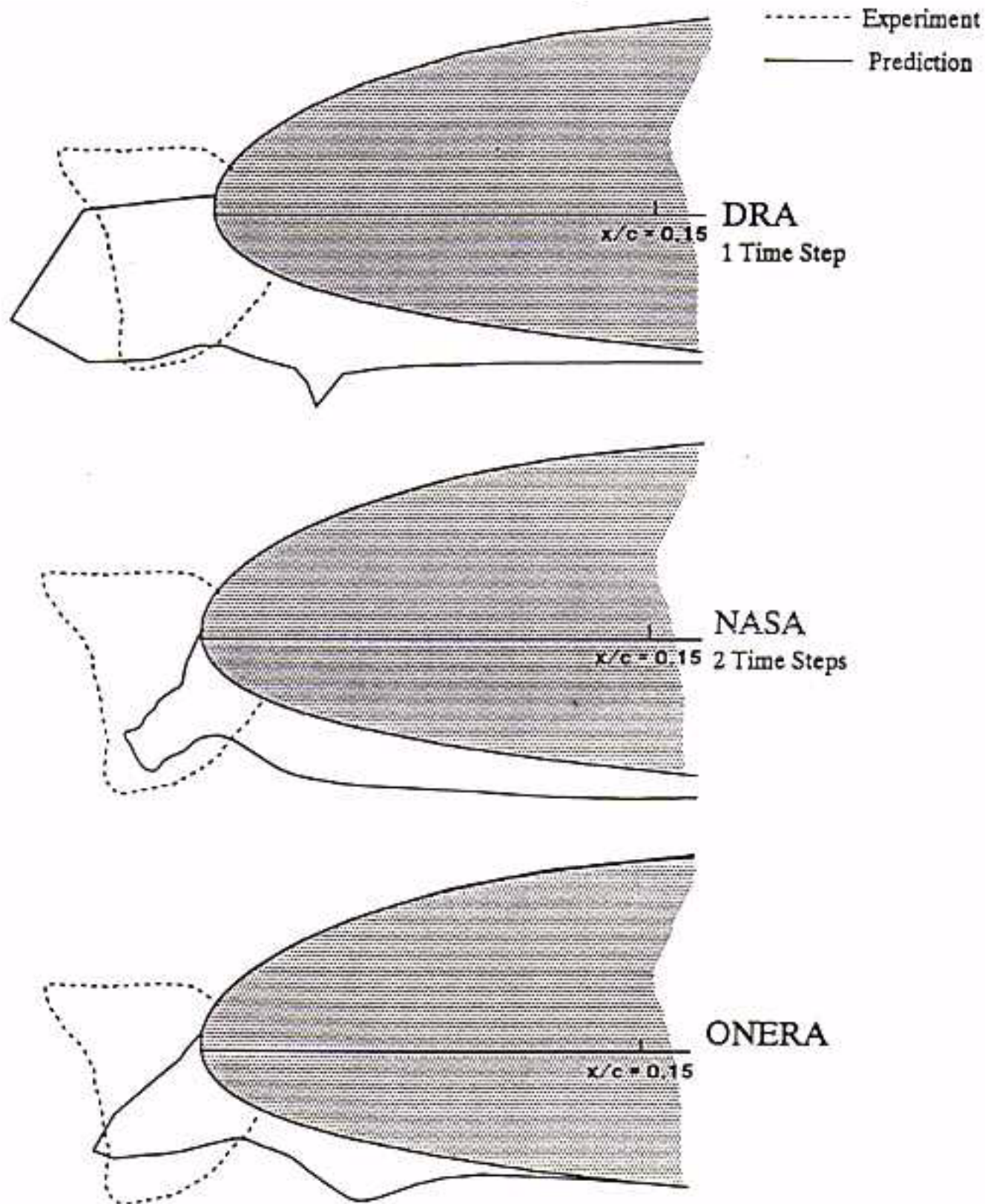


Figure 40A - Comparison of ice shape predictions for ONERA cases.

SA13112, Chord = 0.6, $\alpha = 10.0$, $M = 0.25$, $T_s = -10.0^\circ\text{C}$, $LWC = 0.5$, $MVD = 20.0\mu$, $r = 900.0$

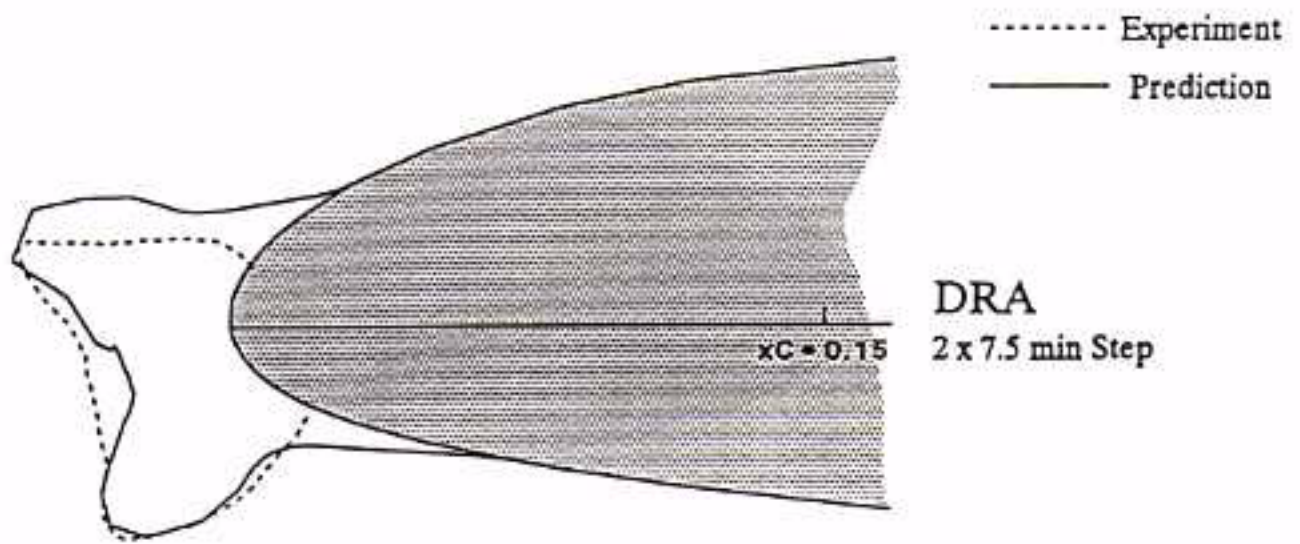


Figure 40B - Comparison of ice shape predictions for ONERA cases.

SA13112, Chord = 0.6, $\alpha = 2.0$ (stalled), $M = 0.25$, $T_s = -10.0^\circ\text{C}$, $LWC = 0.5$, $MVD = 20.0\mu$, $\tau = 900.0$

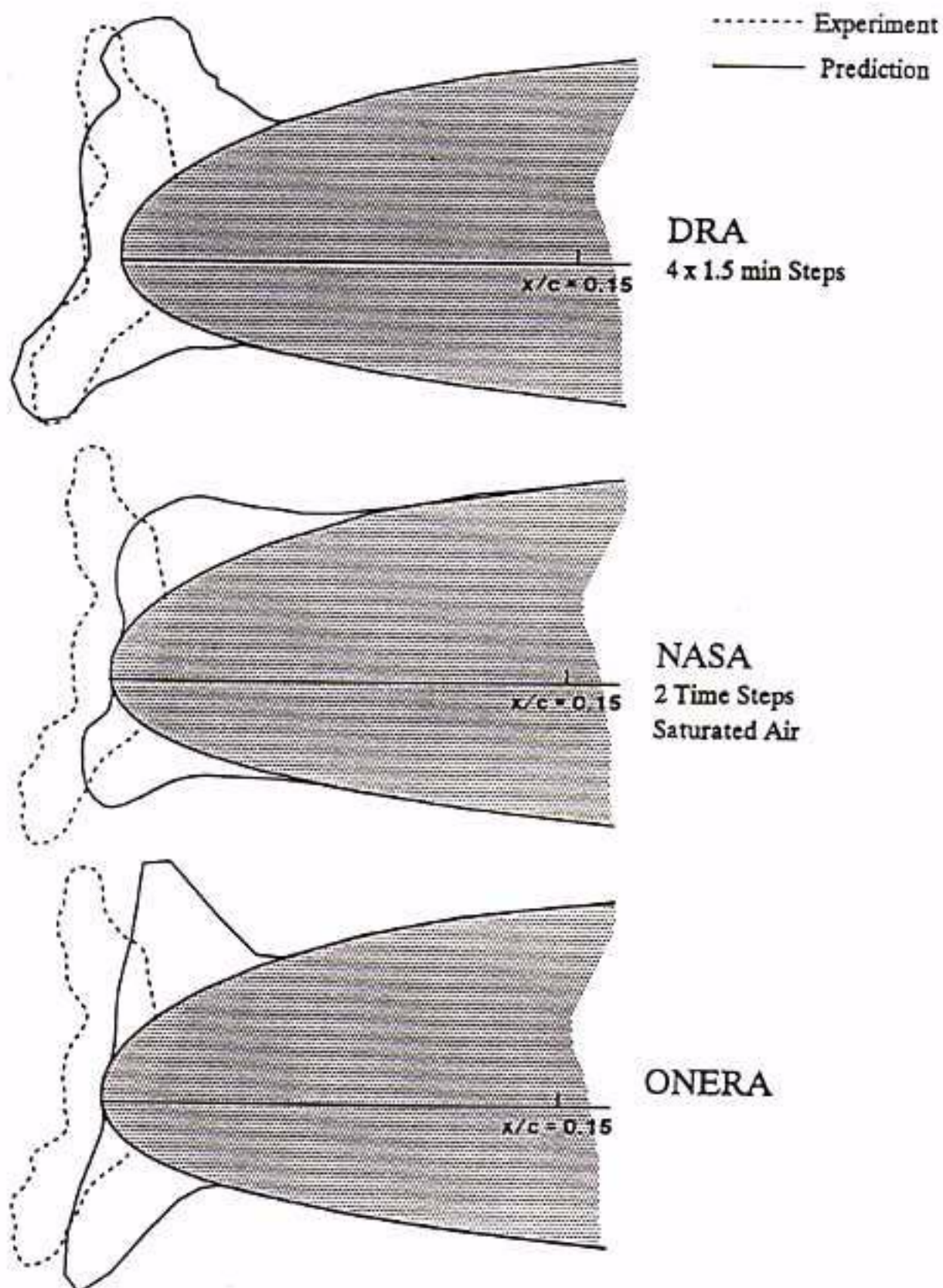


Figure 41 - Comparison of ice shape predictions for ONERA cases.

SA13112, Chord = 0.6, $\alpha = 0.0$, $M = 0.50$, $T_s = -10.0^\circ\text{C}$, $LWC = 0.5$, $MVD = 20.0\mu$, $\tau = 450.0$

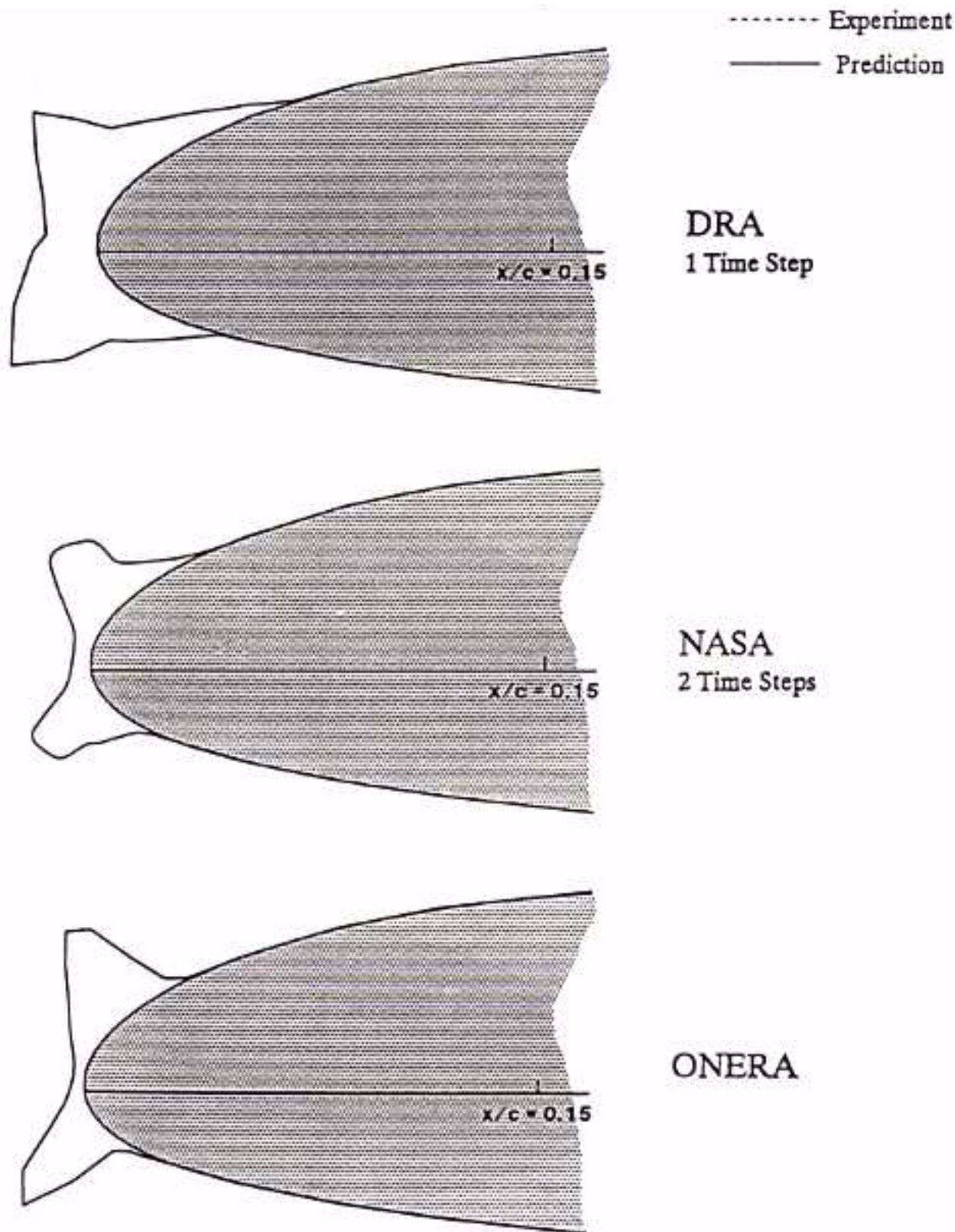


Figure 42 - Comparison of ice shape predictions for ONERA cases.

SA13112, Chord = 0.6, $\alpha = 0.0$, $M = 0.80$, $T_s = -30.0^\circ\text{C}$, $LWC = 0.5$, $MVD = 20.0\mu$, $\tau = 180.0$